JOURNAL OF GEOPHYSICAL RESEARCH, VOL. 97, NO. C7, PAGES 11,411–11,427, JULY 15, 1992

Sea Surface Mean Square Slope From K_u-Band Backscatter Data

F. C. JACKSON, W. T. WALTON,[1] AND D. E. HINES

NASA Goddard Space Flight Center, Greenbelt, Maryland

B. A. WALTER[2]

Pacific Marine Environmental Laboratory, National Oceanic and Atmospheric Administration, Seattle, Washington

C. Y. PENG

Science Systems and Applications, Incorporated, Lanham, Maryland

Near-nadir, quasi-specular backscatter data obtained with a 14-GHz airborne radar altimeter are analyzed in terms of the surface mean square slope (mss) parameter. The raw mss data, derived from a least squares fitting of a ray optical scattering model to the return waveform, show an approximately linear wind speed dependence over the wind speed range of 7–15 m s^{-1}, with a slope of about one half that of the optically determined mss. Further analysis based on a simple two-scale scattering model indicates that, at the higher wind speeds, ~20% of this apparent slope signal can be attributed to diffraction from waves shorter than the estimated diffraction limit of ~0.10 m. The present slope data, as well as slope and other data from a variety of sources, are used to draw inferences on the structure of the high wavenumber portion of the wave spectrum. The data support a directionally integrated model height spectrum consisting of wind speed dependent $k^{-5/2}$ and classical Phillips' k^{-3} power law subranges in the range of gravity waves, with a transition between the two subranges occurring around 10 times the peak wavenumber, and a Durden and Vesecky wind speed dependent spectrum in the gravity-capillary wave range. With a nominal value of the spectral constant $A_u = 0.002$ in the first $k^{-5/2}$ subrange, this equilibrium spectrum model predicts a mss wind speed dependence that accords with much of the available data at both microwave and optical frequencies.

1. INTRODUCTION

A knowledge of the distribution of wave slopes in the sea is important for understanding a number of processes occurring at or near the air-sea interface. The internal dynamics of the wave field, including wave breaking and nonlinear energy transfer among wavenumbers is a strong function of wave steepness of both the energy-containing and the high-frequency waves [*Longuet-Higgins*, 1978; *Phillips*, 1985; *Resio and Perrie*, 1991]. Form drag generated by wave slopes affects the aerodynamic roughness of the sea surface and the turbulent exchange characteristics of the surface layer [*Munk*, 1955; *Jahne*, 1987; *Wu*, 1987; *Janssen et al.*, 1989; *Geernaert*, 1990; *Donelan*, 1990; *Chalikov and Makin*, 1991]. The scattering of light, radio, and acoustic waves by the sea surface depends on the slope distribution, either directly, as in the case of quasi-specular scattering [e.g., *Barrick*, 1974; *Jackson*, 1979], or indirectly, via tilting and hydrodynamic effects, as in the case of large-angle, Bragg diffraction scatter [*Durden and Vesecky*, 1985; *Plant*, 1986; *Donelan and Pierson*, 1987; *Weissman*, 1990].

For many of these processes and applications, one needs to know the distribution of wave slopes over a wide range of surface wavenumbers. *Cox and Munk*'s [1954] remote scattering method represents one of the few practical means of obtaining such data. Their now classical measurements of the slope probability density function (pdf) and mean square slope (mss) parameter using the Sun's natural glint still constitute an extraordinarily useful surface set, one that despite some criticism [*Wentz*, 1976] has yet to be contradicted by new data [*Haimbach and Wu*, 1985; *Hwang and Shemdin*, 1988].

Microwave quasi-specular scattering measurements similar to Cox and Munk's optical measurements also date back to the 1950s. Most of the early work was based on an exact ray optic, or geometrical optics (GO) analogy [cf. *Beckmann and Spizzichino*, 1963, p. 404; also, *Barrick*, 1974; *Brown*, 1979]. In the exact analogy, the microwave backscatter cross section σ^0 for nearly vertically incident radiation is proportional to the wave slope pdf, where the wave slope satisfies the condition for specular reflection of the incident wave. Although not explicitly modeled, diffraction is assumed to play a role in the scattering by limiting the short wavelength response to the order of a few electromagnetic (em) wavelengths. While advances in rough surface scattering theory might appear to render this exact analogy antique, it is still a most useful tool from an experimental point of view [*Brown*, 1990].

NASA's airborne scatterometer program, beginning in the late 1960s, has provided much new microwave cross-section data, particularly at K_u-band frequency (~2 cm wavelength), in both small-angle, quasi-specular and large-angle, Bragg diffraction regimes [*Jones et al.*, 1977; *Schroeder et al.*, 1984, 1985]. *Wentz* [1977] analyzed a subset of these data according to a two-scale scattering model and inferred slope

[1]Now at the Engineering Research Center of the University of Maryland.
[2]Now at the Science Applications International Corporation, Bellevue, Washington.

Paper number 92JC00766.
0148-0227/92/92JC-00766$05.00.

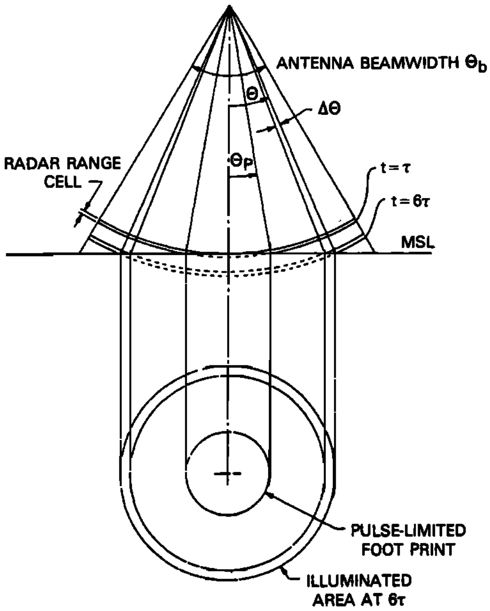

Fig. 1. ROWS altimeter mode measurement geometry [from *Hammond et al.*, 1977].

pdf as well as small-scale roughness parameters. More recently, Japanese scatterometer measurements at X band (~3 cm) have been analyzed for the mss parameter according to the GO model [*Masuko et al.*, 1986]. Satellite passive microwave data at several frequencies have also provided estimates of the mss parameter according to both GO [*Wilheit*, 1979] and two-scale models [*Wentz*, 1975] of the surface emissivity. A wealth of K_u-band, quasi-specular scatter data presently exists as a result of NASA and U.S. Navy satellite altimeter and scatterometer programs [*Fedor and Brown*, 1982; *Schroeder et al.*, 1982; *Dobson et al.*, 1987; *Witter and Chelton*, 1991]. However, as yet, most of these data have not been analyzed in terms of the surface slope statistics, and so their usefulness to air-sea interaction research has been limited.

This contribution attempts to remedy this situation by presenting a synopsis of available slope data. Motivation has been supplied by a new set of K_u-band frequency, quasi-specular scatter data that we have obtained with a short-pulse radar altimeter under well-documented surface conditions. These observations are reported in the next section. Since, as will be seen, the observations support no more than a Gaussian surface, GO interpretation, they are first analyzed accordingly (in section 2). Diffraction and distribution peakedness effects are accounted for subsequently in section 3. Section 4 compares the new mss data with other available mss data. The available data are then rationalized and discussed in terms of a model of the wave spectrum in sections 5 and 6.

2. Observations of the mss With a Broad-Beam Altimeter

Measurements of the mss have been made with the NASA K_u-band, airborne "radar ocean wave spectrometer" (ROWS) instrument [*Jackson et al.*, 1985] operating in a nadir-looking "altimeter" mode according to a technique described in *Hammond et al.* [1977]. As depicted in Figure 1, a relatively broad beam width radar altimeter situated at some altitude H above the mean sea surface transmits a short pulse of duration T_p at some time $t = 0$, say. If the surface is flat, the first signal return, from the nadir point, occurs at time $t_o = 2H/c$, where c is the speed of light. For subsequent delay times, the backscatter comes from angles off nadir given by

$$\tan \theta \approx [c(t - t_o)/H]^{1/2} \tag{1}$$

The angular resolution is poorest at nadir, where it is given by $\Delta\theta = \theta_p = (cT_p/H)^{1/2}$; it improves rapidly with time from the nadir point. For the ROWS, the half power width of the Gaussian-shaped pulse is $T_p = 12.5$ ns. Assuming an azimuthally integrated cross section that is approximated by the isotropic, Gaussian surface, GO form [e.g., *Valenzuela*, 1978; *Barrick*, 1974]:

$$\sigma^o_{\text{GOG}} = \rho_g(\sec^4 \theta/m_g^2) \exp(-\tan^2 \theta/m_g^2) \tag{2}$$

where ρ_g is an effective reflectivity and m_g^2 is an effective mss parameter, and assuming also a Gaussian approximation to (the main lobe of) the antenna pattern, then the average backscattered power as a function of delay time can be shown [*Barrick*, 1972; *Hammond et al.*, 1977] to be given approximately by

$$W(t) = (A/2)\{1 + \text{erf}[(t - t_o)/2^{1/2}\sigma]\} \exp[-(t - t_o)/\tau] \tag{3}$$

where A is the waveform amplitude and σ and τ are the leading and trailing edge parameters given by

$$\sigma = (4\sigma_h^2/c^2 + \sigma_p^2)^{1/2} \tag{4}$$

$$\tau = (H/c)(1/m_g^2 + 1/\sigma_b^2)^{-1} \tag{5}$$

where σ_h^2 is the wave height variance, σ_p is the one sigma pulse width parameter, and σ_b is the one sigma beam width parameter $\sigma_b = 0.424\ \theta_b$ where θ_b is the half power beam width. (Note that in writing (3), some additional terms given by *Barrick* [1972] and by *Hammond et al.* [1977] have been suppressed; if these terms were to be expressed explicitly, then we should have $A \to A \exp[-(\sigma/\tau)^2/2]$ and $t_o \to t_o - (\sigma^2/\tau)$). Since the slope pdf at microwave frequencies is quasi-isotropic (Appendix A), adoption of the isotropic form (2) of the azimuthally integrated cross section at most involves an error of a few percent in the estimation of the mss parameter. The above equations define ρ_g and m_g^2 operationally as "gross fit" parameters that provide a best fit, say, in a least squares sense, of the model function (3) to the observed waveform. On account of diffraction from small-scale surface structure, ρ_g may be expected to differ from the normal incidence K_u-band Fresnel reflectivity of $\rho_o \sim 0.62$ that would apply in the absence of small structure.

ROWS altimeter-mode measurements were made in the Mesoscale Air-Sea Exchange (MASEX) experiment [*Chou et al.*, 1986] and in the Frontal Air-Sea Interaction Experiment (FASINEX) [*Weller*, 1991]. In the first experiment the radar was equipped with a small nadir-directed, standard gain horn antenna (Waveline model 799), herein denoted by H2. The 3-dB full beam width of this antenna is $\theta_b = 32.4° \pm 0.7°$ as determined by manufacturer, laboratory, and antenna range pattern measurements, where θ_b is taken to be the geometric mean of measured E and H plane beam widths. The $\pm 0.7°$ beam width uncertainty results, according to (5), in a mss measurement uncertainty $\Delta m_g^2 / m_g^2 = \pm 0.8 m_g^2$. For small mss values, $m_g^2 = 0.025$, say, the mss uncertainty is around $\pm 2\%$, while for relatively large mss, $m_g^2 = 0.05$, say, this uncertainty increases to around $\pm 4\%$. The observations in MASEX were made from a NASA P-3 aircraft operating at 1300 and 6400 m altitudes. Wind and other surface boundary layer measurements were made by a National Oceanic and Atmospheric Administration WP-3D gust probe aircraft flying at 50 m altitude. In FASINEX the radar was operated with two nadir-pointing antennas: the H2 antenna, aforementioned, and an open circular waveguide fitted with an RF choke, herein denoted H1. To eliminate the possibility of a bias between the H1 and H2 data caused by small relative beam width specification errors, we have used an H1 beam width parameter based on geophysical comparison involving the differencing of the measured trailing edge parameters (inverse values of τ) from adjacent H1 and H2 files assuming a constant mss between them. From 13 such comparisons the H1 beam width value was determined to be $\theta_b = 53.7° \pm 3°$. Most of the altimeter mode data in FASINEX were obtained with the H1 antenna at 450 m altitude while flying in tandem with the National Center for Atmospheric Research Electra gust probe aircraft operating at 40 m altitude. Supporting wind and boundary layer data in FASINEX were also provided by the research vessels *Oceanus* and *Endeavor* [*Pennington and Weller*, 1986].

Return waveforms were sampled at either 2- or 5-ns resolution with 6-bit quantization and recorded in 256-word frames at the 100-Hz radar pulse repetition frequency. Files of a minimum of 30-s duration were processed as follows: After bias subtraction, epoch times t_o were estimated from 1-s average data as the time of 60% of the peak value and then filtered using a five-point triangular filter. Individual pulse returns for the record were then realigned according to the filtered epoch (altitude) signal. Finally, the realigned waveforms were averaged in 10-s subfiles and subjected to an iterative least squares fit (LSF) of the model waveform (3) to the data for the four parameters A, σ, τ, and t_o, where the fit window extends either to the end of the record or to about 10% of the peak value.

In MASEX the radar gain was set to give an average peak return signal that was about 30% of the full scale of the Biomation 6500 digitizer. This resulted in approximately 5% of the individual pulse returns saturating in the peak region. If we assume hard limiting of the digitizer at the 64th level and exponential fading statistics for the individual pulse return, then it follows that the measured average return power is

$$\langle W_{\text{meas}} \rangle = W_o[1 - \exp(-63/W_o)] \qquad (6)$$

where $W_o = W_o(t)$ is the true average power. The MASEX average waveform data have been corrected according to (6) using a table look-up procedure. In FASINEX a lower system gain was used and average peak signal levels were 10–15% of the full scale of 0–63 counts; thus no saturation correction was necessary for these data.

Figure 2 depicts the leading edge region of 1-s averaged waveforms from a 30-s file of data from MASEX. The altitude variation caused by aircraft vertical motion evident in this figure is typical of the data collected from the P-3 platform. Figure 3 is a typical example of a (saturation-corrected) 10-s average waveform and the corresponding model waveform LSF. As can be seen, the waveform fit is quite good in both the leading and trailing edge regions, with rms residuals amounting to no more than 1–2% of the waveform amplitude. For the higher altitude data, it follows that mss estimates obtained from 10-s records are very stable, since a large number of independent backscatter samples go into an mss estimate (e.g., around 10^5 = 1000 pulses × 100 range cells at 6 km altitude) and since the surface area viewed is quite large. At the lower (450 m) altitude, however, sampling variability, mainly geophysical, is significant for the 10-s records, and so several 10-s subfiles must be averaged for stable estimates of both rms wave height and mss.

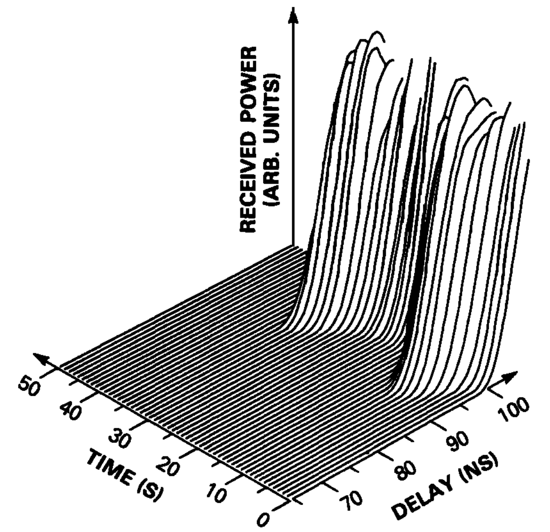

Fig. 2. Time history of return pulses in leading edge region (consisting of 1-s average waveforms) illustrating epoch variation caused by aircraft vertical motion.

Table 1 lists the mss data and 10-m equivalent neutral wind speed (U_{10n}) and surface friction velocity (u_*) data from the aircraft and shipboard measurements. Figure 4 shows the observed mss as a function of U_{10n} and u_*. The aircraft u_* were determined according to the eddy correlation method while the shipboard u_* were determined according to the dissipation method [see *Friehe et al.*, 1991; *Li et al.*, 1989; *Large and Businger*, 1988; *Davidson et al.*, 1987]. In the cases where multilevel stack data were available, the measured eddy stresses at the 40–50-m flight levels were extrapolated to the surface using the observed profiles of the stress. Otherwise, the surface u_* were estimated by adding 5% to the measured flight level values. The flight level winds were reduced to neutral 10-m winds using the measured u_* in the standard Monin-Obukhov boundary layer model for the mean wind,

$$U(z) = (u_*/K)[\ln(z/z_o) - \psi(z/L)] \qquad (7)$$

where the von Karman constant $K = 0.40$ and the stability function ψ is computed according to a modified Businger-Dyer relationship using the 50-m level measured fluxes of virtual temperature for the stability length L [cf. *Large and Pond*, 1981, equation 7] with the numerical value 16 replaced by 28. Comparison of the measured u_* for MASEX with the

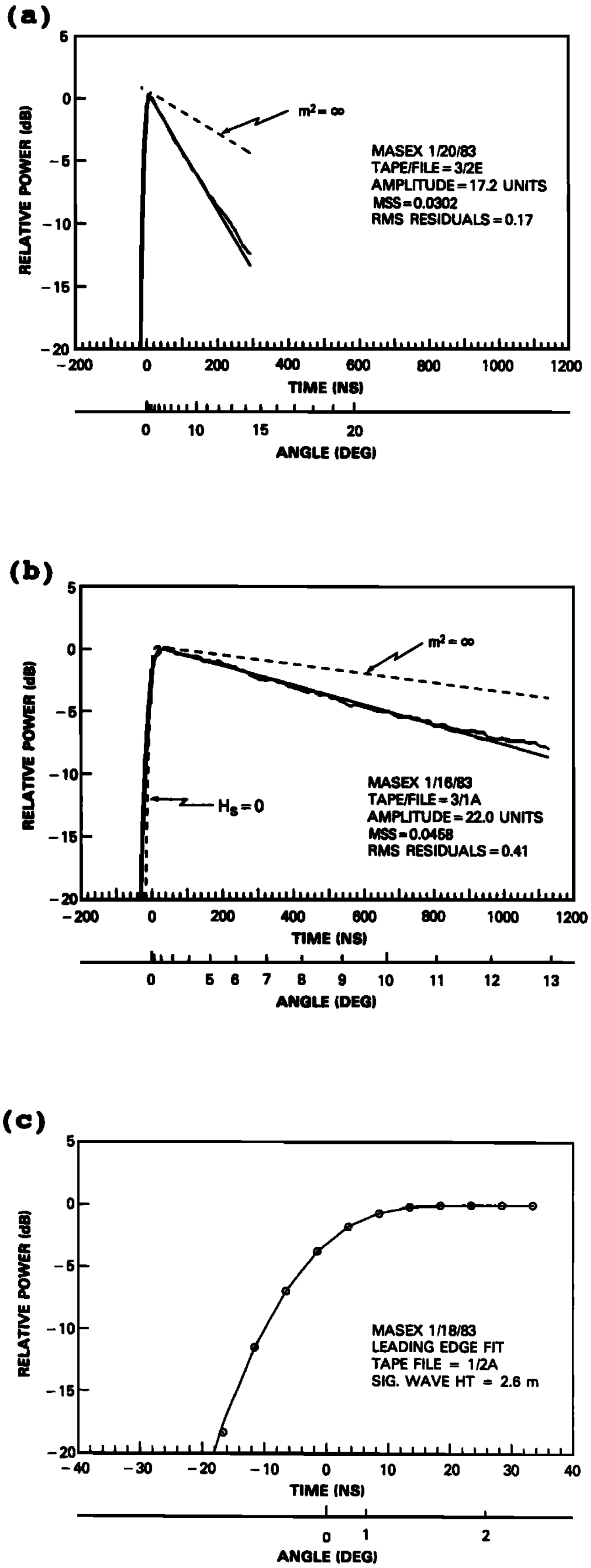

Fig. 3. Examples of waveform model fits to 10-s average power data: (*a*) low-altitude, small-mss case, (*b*) high-altitude, large-mss case, and (*c*) special fit to leading edge region. Note that the fits were performed on the actual relative power rather than on log power.

boundary layer model predictions of *Cardone* [1969] and *Large and Pond* [1981], using the measured air-sea temperature differences ($-7°$ to $-14°$C), shows them to be in good agreement with the Cardone model for the higher wind speeds (12–14 m s^{-1}), but somewhat larger than the Large and Pond model values, as indicated in Figure 4*b*. It is seen from Figure 4 that the diffraction effective, or gross fit K_u-band mss m_g^2 has an approximately linear wind speed and friction velocity dependence between 7 and 15 m s^{-1} wind speeds, with slopes of about half of the corresponding optical mss data as determined by *Cox and Munk* [1954] (cf. section 4.3). Linear regressions on the data, as shown in Figure 4, give

$$m_g^2 = 0.0023\ U_{10n} + 0.013 \pm 0.002 \tag{8}$$

for 7 m s^{-1} $< U <$ 15 m s^{-1}

and

$$m_g^2 = 0.041\ u_* + 0.021 \pm 0.002 \tag{9}$$

for 0.20 m s^{-1} $< u_* <$ 0.60 m s^{-1}.

The correlation coefficients are 0.96 and 0.91, respectively, for the two data sets.

3. Diffraction and Peakedness Effects

Diffraction effects are analyzed here according to a two-scale (denoted as 2S in the equations) model approximation to the physical optics (PO) integral for scattering from a perfectly conducting sea surface. The analysis is intended to provide a framework for interpreting the raw, or gross fit mss data m_g^2, in terms of filtered surface slope variance $m_f^2(k_d)$ and diffuse scatter contributions in such a way that the appropriate scale separation, or diffraction limit wavenumber k_d, is objectively determined. While limited by the perfect conductivity assumption, this approach is at least self-consistent and well justified in terms of the known properties of the PO integral in the perfect conductivity case, as discussed in Appendix B (and see comments concluding this section).

As shown in Appendix B, the two-scale approximation to the PO integral form of the cross-section σ_{PO}^0 is given by $\sigma_{2\mathrm{S}}^0 = \sigma_{\mathrm{GOF}}^0 + \sigma_{\mathrm{DIF}}^0$, where $\sigma_{\mathrm{GOF}}^0 = \rho_f \pi \sec^4\theta\, p_f(\mathbf{s})$ is the GO cross section for the low-pass filtered surface, where ρ_f is a reduced normal incidence reflectivity and p_f is the slope pdf of the filtered surface, $\mathbf{s} = \tan\theta\,(\cos\phi, \sin\phi)$, being the specular slope vector; and where the diffuse diffraction term σ_{DIF}^0 is given by (B3). In the case of an isotropic, Gaussian surface, σ_{GOF}^0 is given by the same form (2) used in the empirical data fits but with the gross fit reflectivity and mss parameters replaced by the "filtered surface" parameters ρ_f and m_f^2. In terms of the surface height spectrum $F(\mathbf{k})$ the filtered surface mss is given by

$$m_f^2 = \int_0^{|\mathbf{k}| = k_d} |\mathbf{k}|^2 F(\mathbf{k})\, d\mathbf{k} \tag{10}$$

We use the PO integral form (B5) for the isotropic, Gaussian surface case to analyze the two-scale approximation and determine the diffraction limit. We solve for the free parameter k_d similarly to *Thompson* [1988] by minimizing the

TABLE 1. ROWS Altimeter Mode Data

Date	Tape/File (Subfiles)	Start Time, UT	Altitude, m	Antenna	Gate, ns	$H_{1/3}^a$, m	U_{10n}, m/s	u_*, m/s	mss	Comments
					MASEX (1983)					
Jan. 16	3/1 (1—5)	1821:44	6462	H2	5	4.5	13.9	0.59	0.045	Large fetch, wave age $c/U_{10} \sim 1$; $T_{air} - T_{sea} = -8.6$°C; U_{50} = 14.8 m/s
Jan. 18	1/2 (1–4)	1745:34	6324	H2	5	2.5	12.1	0.56	0.041	Moderate fetch, $c/U_{10} \sim 0.7$; $T_{air} - T_{sea} = -14.3$°C; U_{50} = 12.5 m/s
Jan. 20	3/1 (1–4)	2317:00	1368	H2	2	1.1	>7.9	···	0.032	Sea fully developed
	3/2 (1–5)	2318:29	1365	H2	2	1.4	7.9	0.20	0.030	$T_{air} - T_{sea} = -6.9$°C
	3/3 (1–5)	2324:30	1369	H2	2	1.2	<7.9	···	0.028	U_{50} = 7.5 m/s
					FASINEX (1986)					
Feb. 18	3/1 (1–24)	1731:44	470	H1	2	1.5	8.7	0.34	0.031	*Electra* winds and u_* warm side of front; swell dominated conditions [see *Li et al.*, 1989]
	3/5 (1–14)	1741:30	452	H1	2	1.3	8.1	0.25	0.030	*Electra* winds and u_* cold side of front
Feb. 20	3/3 (1–11)	1702:30	440	H1	5	2.2	12.5–	0.54–	0.047	1700–1735Z *Oceanus* winds and u_* 25 km downstream; inhomogeneous conditions
	3/5 (1–9)	1208:54	435	H1	5		16.0	0.60	0.047	Squalls
Feb. 21	4/1 (1–12)	1545:31	445	H1	2	2.9	11.3–	0.35	0.040	1500–1530Z *Oceanus* winds and *Electra* u_*; falling winds; predominantly swells
	4/3 (1–17)	1552:27	447	H1	2	2.9	8.9	0.38	0.038	See *Liu et al.* [1989]
Feb. 24	4/7 (15–27)	1616:25	460	H1	5	···	9.2	···	0.034	1630 *Oceanus* wind and *Endeavor* wind 1700Z
	5/1 (31–39)	1642:58	460	H1	5	···	8.7	···	0.035	
Feb. 26	5/1 (1–13)	1930:15	460	H1	5	5.3	14.5	···	0.043	1930 *Oceanus* winds; fully developed seas

[a] $H_{1/3} = 4\,\sigma_h$; MASEX wave heights from waveform leading edge model fit ±30 ns of the epoch; FASINEX wave heights from the surface contour radar or laser profiler.

difference between the PO integral and the two-scale approximation to it. We may consider either minimizing the difference for a given incidence angle or, more appropriately in our case, we may consider the value of k_d found by LSF of σ_{2S}^o to the parent PO form (B5) over an angular range comparable to that used in the data analysis of section 2. Since the data are analyzed nominally over the range $\theta \leq \arctan 3^{1/2}m$, where m^2 is a nominal value of the mss, we similarly seek a value of k_d such that

$$d/dk_d \int_0^{3m^2} [\sigma_{2S}^o(\theta;\, k_d) - \sigma_{PO}^o(\theta)]^2\, d(\tan^2\theta) = 0 \qquad (11)$$

We calculate k_d for the specific case of a Phillips spectral law surface, $F = (B/2\pi)k^{-4}$, $k > k_o$ and $F = 0$ otherwise, where k_o is the peak wavenumber. For intermediate wind speeds (around 10 m s^{-1}), this simple model of the spectrum may be taken as fair approximation to the actual spectrum at high wavenumber [*Jähne and Riemer*, 1990, cf. equation 26]. Since the transition from ray optical to diffraction regimes is gradual, the diffraction limit k_d is necessarily a "soft" number, and so not surprisingly, a LSF by analytical partials according to (11) proved to be unstable. Instead of seeking the minimum analytically, we simply graph the integral in (11) as function of k_d. The result is shown in Figure 5 for parameter values k_{em} = 293 m^{-1} (2.15-cm wavelength), B = 0.005, and $k_o = g/U^2$, where g is the acceleration of gravity and where the wind speed U is varied between 5 and 20 m s^{-1}. From Figure 5, a broad minimum between k_d = 50 and 100 m^{-1} is evident; narrowed down somewhat, the minimum occurs between k_d = 60 and 80 m^{-1}, approximately. The results for k_d versus incidence angle for a given wind speed are given in Figure 6. Particularly note that at nadir, $k_d \sim 70$ m^{-1}. Since these results scale with the em propagation constant k_{em}, one may conclude, on the basis of this analysis, that the diffraction limit is of the order of 3–6 wavelengths. With k_d values in this range the small curvature and small Rayleigh number criteria for the large-scale and small-scale surfaces, respectively, are well satisfied [cf. *Brown*, 1978; *Durden and Vesecky*, 1985]. Values of k_d estimated by other authors are listed in Table 2. Many of these estimates are close to the present estimate.

Figure 7 compares the two-scale model fit to the parent PO integral assuming a value of k_d = 80 m^{-1}. In this comparison, both PO and two-scale cross section models are normalized by the GO cross-section form (2) that best fits the PO integral (B5) in the same least squares sense as (11). It is seen from Figure 7 that the two-scale model approximates the PO integral fairly well over the angular range $\theta \leq \arctan 3^{1/2}m$. Residuals are of the order of a few percent.

For a wind speed dependent spectrum, k_d may be expected to vary with wind speed. However, it will be seen that the model results for m_g^2 are not very sensitive to the precise value k_d for the reason that an increase or decrease of m_f^2 with varying k_d is largely compensated for in the apparent mss m_g^2 by commensurate changes in the contribution from the diffuse diffraction field. Subsequently, in section 6, we will use the above simple diffraction model to develop the relationship between m_f and m_g for a given wind speed dependent model spectrum.

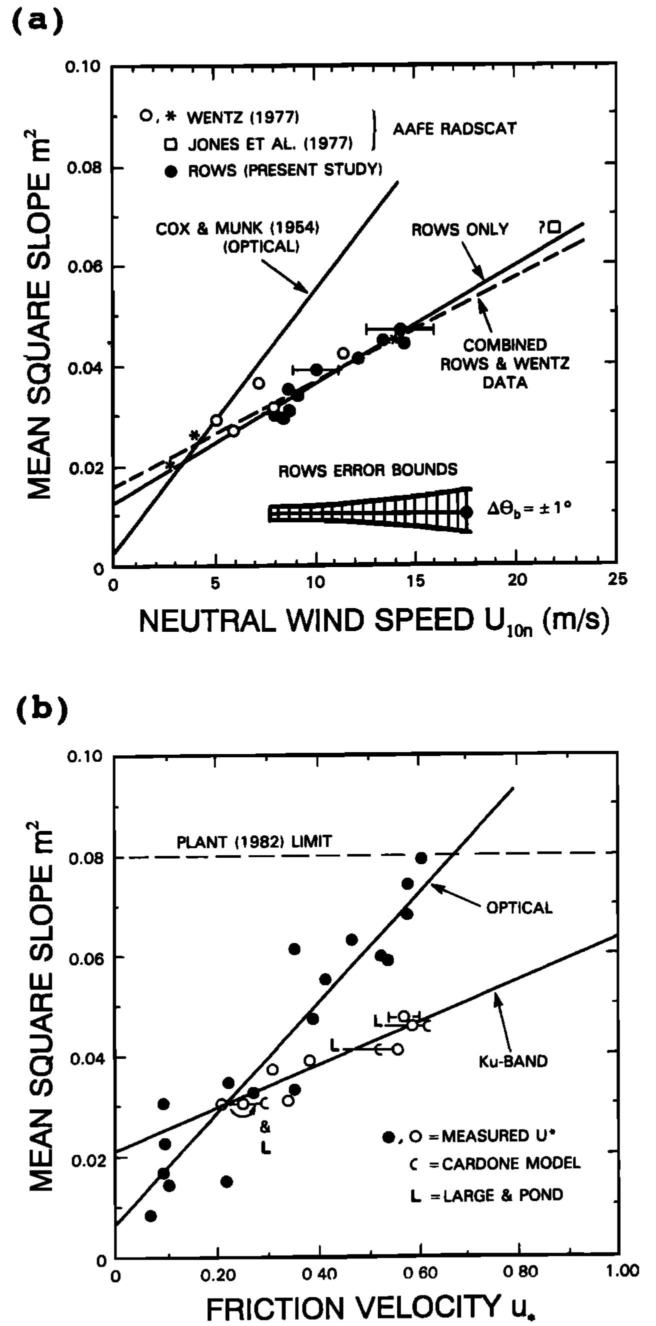

Fig. 4. (*a*) Mean square slope versus equivalent 10-m neutral wind speed with regression lines for ROWS mss alone and for combined ROWS and *Wentz* [1977] data sets (open circles indicate JONSWAP '75 data, and asterisks indicate other mission data) with optical regression result shown for comparison. Note that the high wind speed data point from *Jones et al.* [1977] is not included in the regressions. (*b*) ROWS slope data versus measured and model-predicted friction velocity, with optical data from *Cox and Munk* [1954] shown for comparison.

Unmodeled slope distribution peakedness also affects the measured mss. Since distribution peakedness will generally cause the distribution to be narrower over the extent of the data window, the result will be an underestimate of the mss. Since skewness to first order vanishes in the azimuthally integrated cross section case, one may express the equivalent isotropic GO cross section by [e.g., *Cox and Munk*, 1954]

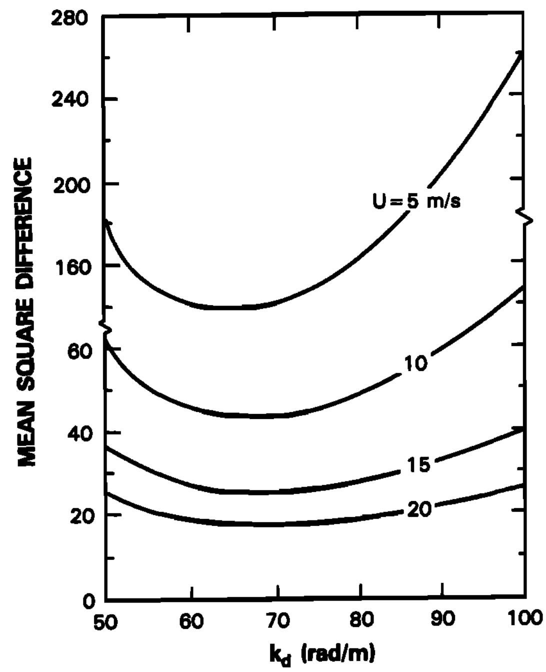

Fig. 5. Mean square difference between the physical optics (PO) integral and two-scale model approximation over the angular range $\theta = 0 - 3^{1/2}\, m$ as a function of the scale wavenumber k_d for four wind speeds (U) assuming a Phillips spectrum with low wavenumber cutoff $k_o = g/U^2$.

$$\sigma^o_{GO} = (\rho \sec^4 \theta/m^2) \exp(-\bar{s}^2)[1 + (c_{40}/6)(\bar{s}^4 - 4\bar{s}^2 + 2)] \tag{12}$$

where $\bar{s} = s/m$, $s = \tan\theta$ as before; where c_{40} is the peakedness coefficient defined by *Cox and Munk* [1954]; and where the subscripts "F" or "G" may further be attached

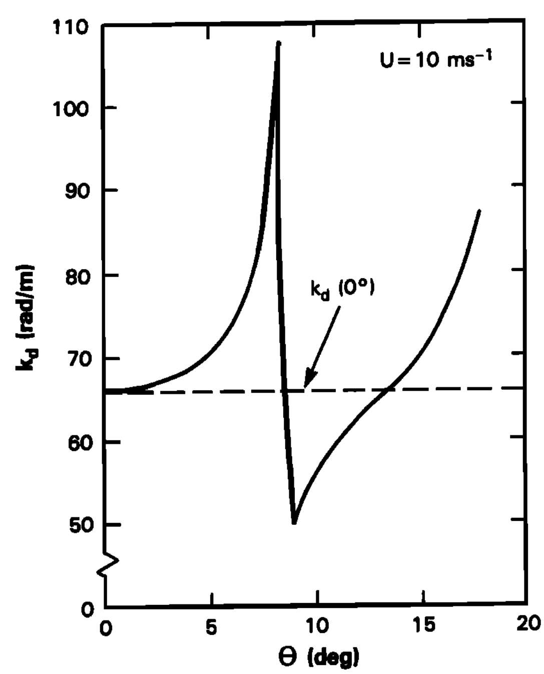

Fig. 6. Scale separation wavenumber k_d as a function of incidence angle θ.

TABLE 2. Estimates of the Scale Separation Wavenumber k_d

	k_d/k_{em}	k_d, m^{-1}	Comments
Wentz [1977]	1.5	193 ± 50	Two-scale model fits to aircraft data around θ = 20° (finite conductivity)
Durden and Vesecky [1985]	5	···	Rayleigh parameter less than 0.5; all θ
Brown [1978]	3	···	Rayleigh parameter equals 0.1; all θ (perfect conductivity)
Donelan and Pierson [1987]	40	···	Arbitrary; primarily Bragg regime
Plant [1986]	5–10	···	Arbitrary; primarily Bragg regime
Thompson [1988]	3	···	Two-scale model fit to PO integral, θ = 23° (perfect conductivity)
Present study	3–6	50–100	Two-scale model fit to PO integral, θ < 15° (perfect conductivity)

to σ^o_{GO} depending on whether the GO form refers to the filtered surface or gross fit case. According to *Wentz'* [1977] data, c_{40} = 0.20 ± 0.30. Assuming a nominal value of c_{40} = 0.20, if follows from (12) that unmodeled peakedness will result in an underestimate of the mss inferred from a nadir sigma-zero measurement, which type of mss retrieval will be denoted by m_n^2 to distinguish it from the shape-based or gross fit mss m_g^2 (cf. equation 13 below), by about 6%. From numerical simulation we find that peakedness affects the gross fit mss m_g^2 computed according to the Gaussian model (2) by approximately the same amount when the fit window is taken to be $0 \le \tilde{s} \le 3^{1/2}$.

Finite conductivity effects may be accounted for an ad hoc fashion by letting $\rho_f = \rho_o \rho_f^*$ and likewise for the "g" and "n" subscripted reflectivities where subscripts g and n refer to mss retrievals from relative cross-section shape and absolute value of the cross section at nadir, respectively (cf. equations (2) and (13)) where ρ_o is the Fresnel normal incidence reflectivity (equal to 0.62 at K_u-band) and where the asterisk connotes the perfect conductivity value as described in Appendix B. In the case of the filtered surface

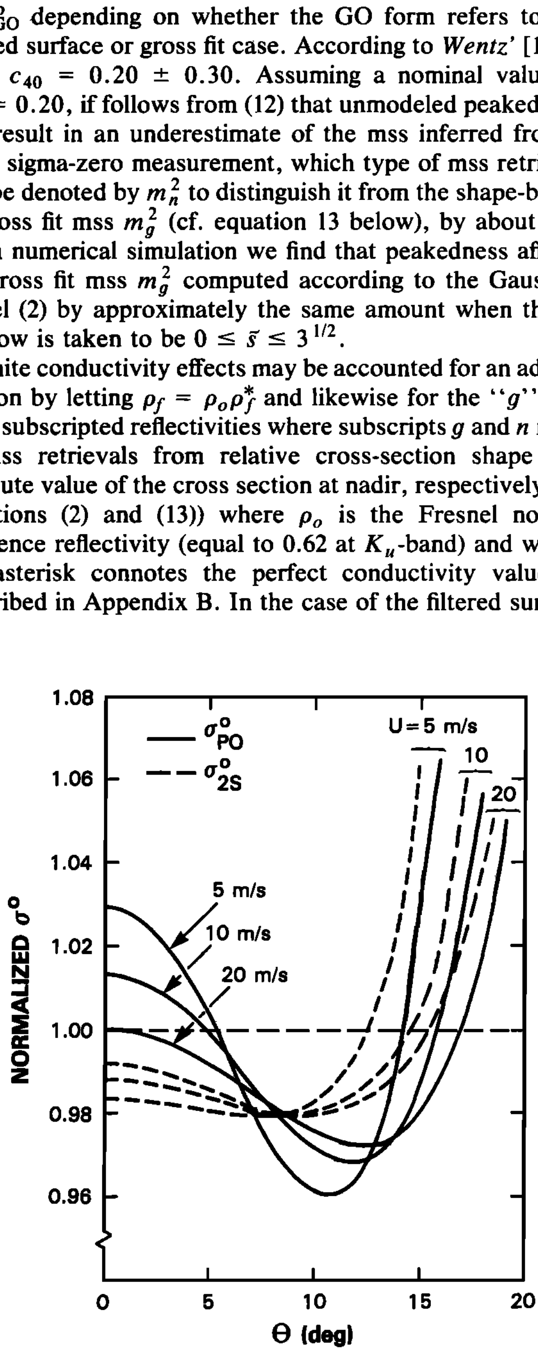

Fig. 7. Physical optics (PO) and two-scale cross sections as a function of incidence angle for Phillips spectrum case assuming k_d = 80 m^{-1}, where both cross sections are normalized by the best fitting geometrical optics cross section to σ^o_{PO} over the indicated angular range.

quasi-specular cross-section term σ^o_{GOF}, this substitution results in an expression identical to the quasi-specular term of *Durden and Vesecky* [1985]. However, we do not claim this finite conductivity form to be rigorous for either the GO or diffraction term [see *Adorjan and Wierum*, 1971, equation 27].

4. Comparison With Other Data

4.1. *Aircraft Data*

The mss from *Wentz'* [1977] two-scale model fits to Advanced Applications Flight Experiment radiometer-scatterometer (RADSCAT) K_u-band scatterometer data [*Jones et al.*, 1977; *Schroeder et al.*, 1984, 1985] are plotted in Figure 4 along with the present ROWS data. For the comparison, Wentz' 19.5-m neutral winds have been converted to 10-m neutral winds according to the approximate relationship, $U_{10n} = 0.93\ U_{19.5n}$. Because *Schroeder et al.* [1984] have questioned the quality of some of the early scatterometer mission data (1973–1974), the Wentz data are segregated according to mission. However, no obvious difference is seen in the data between the suspect early missions and the later JONSWAP 1975 data. The comparison of the Wentz and ROWS mss data in Figure 4 shows good agreement in both level and trend even though the two data sets represent different quantities, namely, $m_g^2(U;\ k_d$ = 60–80 $m^{-1})$ in the case of the ROWS data and $m_f^2(U;\ k_d \sim$ 200 $m^{-1})$ in the case of the Wentz data. That these two quantities should agree despite the different definitions is not unexpected according to the calculations of section 6.

The *Schroeder et al.* [1984, 1985] reanalyzed K_u-band RADSCAT data and *Masuko et al.* [1986] X-band (0.03-m wavelength) data present some problems. While the mss m_n^2 derived from their nadir data according to (13) below with ρ_n' = 0.41 agrees fairly well with the above results, as is evident from Figure 8, the m_g^2 results based on the cross-section shape measurements differ significantly from the previous results. Figure 9 shows the shape-based data, where for the RADSCAT data the mss has been derived from the ratio of nadir to 10° off nadir looks according to the anisotropic GO model (A1), where the data for the two polarizations are averaged and the mss components derived from the upwind/downwind and cross-wind looks are summed. Both data sets exhibit a much lower wind speed response than the ROWS, Wentz, and satellite results (section 4.2 below). The Masuko et al. data are quite low in level and trend compared to the present data; also compared to most of the microwave data summarized by *Beckmann and Spizzichino* [1963, p. 408]. In fact, these mss data are no greater than the *Cox and Munk* [1954] slick surface mss data

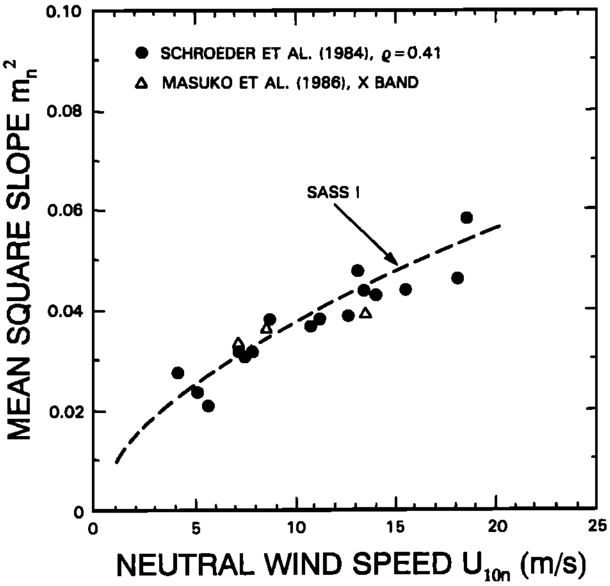

Fig. 8. Inferred mss from AAFE RADSCAT and Japanese X band scatterometer nadir cross-section data with the SASS I curve shown for comparison (reflectivity $\rho'_n = 0.50$ assumed for the SASS I curve and 0.41 for the aircraft data as indicated).

(cf. Figure 14); thus we believe these data are in error. The RADSCAT data are closer to the present results, but the overall wind response is closer to logarithmic than linear. The m_g^2 data from the same flights used by Wentz are comparable to Wentz' m_f^2 results but slightly lower. However, the higher wind speed data from the later missions (numbers 235 and 253) are some 20–40% below the linear regression result (8). Early RADSCAT mission data such as the mission 288 data from *Jones et al.* [1977] that are termed suspect by *Schroeder et al.* [1984], however, show a mss response comparable to the present ROWS data. The apparent discrepancy between the present results and the *Schroeder et al.* [1984] shape-based data needs to be resolved. As noted by *Schroeder et al.* [1984], the 10° incidence cross-section data are surprisingly noisy (variable), and it is possible that this may have something to do with the problem.

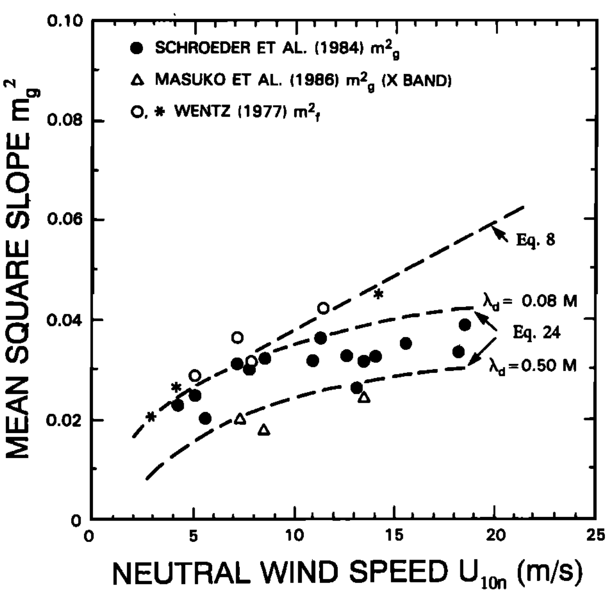

Fig. 9. AAFE RADSCAT and *Masuko et al.* [1986] shape-based mss data compared to present study regression result (equation (8)) and mss from model spectrum (equation (24)) integrated to $k_d = 2\pi/\lambda_d$.

4.2. *Satellite Data*

While aircraft mss measurements can be made on the basis of cross-section shape, this is generally not possible in the case of satellite measurements, as usually only one look at a given incidence angle is possible for a given sea surface area. Consequently, the mss must be inferred on the basis of the magnitude of the cross section at a fixed angle of incidence. Consider the mss implied by the Gaussian surface, GO model of the nadir cross section

$$m_n^2 \equiv \rho'_n/\sigma^\circ(0^\circ) \tag{13}$$

that is, the mss that is implied by (2) for vertical incidence, but with the subscript n here replacing the g subscript to indicate that the value is derived from an absolute power measurement at nadir as opposed to being derived from a gross fit to the cross-section shape over a finite angular range. In section 6 we find from simulations for the perfect conductivity case that if ρ'_n is assumed to be a constant (e.g., $\equiv 1$) then the nadir-inferred mss is almost identical to the shape-based mss, differing only by a small wind speed dependent correction factor as

$$m_n^2 \approx (1 + 0.0025\ U)\ m_g^2 \tag{14}$$

We consider satellite nadir look sigma-zero data sets and the mss implied by (13) when ρ'_n is taken to be some fixed value that makes m_n agree with the aircraft shape-based data over some range of wind speed, say around 7 m s^{-1}. Taken as such, the value attached to the reflectivity may reflect σ^0 calibration error as well as diffraction effects, and so ρ'_n may not necessarily correspond to a true reflectivity (wherefore the added prime notation). Figure 10 shows the mss accordingly inferred from (1) the altimeter wind speed algorithm of *Brown et al.* [1981] (with $\rho'_n \equiv 0.38$ and without the second stage polynomial wind speed correction [see *Fedor and Brown*, 1982; *Dobson et al.*, 1987], (2) the SASS I scatterometer nadir wind speed algorithm for horizontal polarization [*Schroeder et al.*, 1982] (with $\rho'_n \equiv 0.52$), and (3) the modified Chelton-Wentz (MCW) altimeter wind speed algorithm [*Witter and Chelton*, 1991] (also with $\rho'_n \equiv 0.38$) compared to the aircraft ROWS shape-based regression result (8) as modified by (14).

All curves are seen to agree well in the wind speed range of 3–11 m s^{-1}, where the difference between any curve is at most ± 1 m s^{-1} in wind speed. In the intermediate range of wind speeds, between roughly 8 and 11 m s^{-1}, all curves have virtually identical slopes. This agreement continues in the case of the SASS I, MCW, and ROWS curves for wind speeds up to 14–16 m s^{-1}, particularly in the case of the ROWS and MCW curves. Around 11 m s^{-1} the Brown et al. curve shows a rapid increase in mss response that is not reflected in the other curves. This jump in sigma nought and mss, which occurs also in the two-stage Brown et al. algorithm (but at about 10 m s^{-1}) as well as the first-order discontinuity around 8 m s^{-1} is moderated in the "smoothed Brown" algorithm (a fifth-degree polynomial fit) of *Dobson*

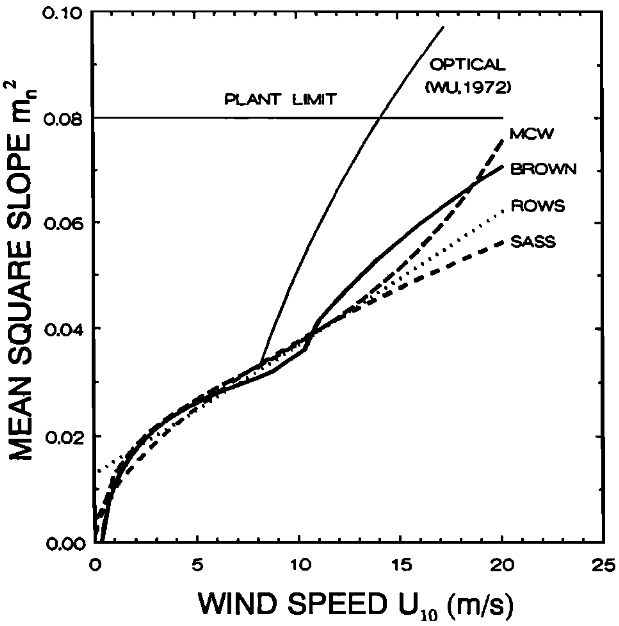

Fig. 10. Inferred mss from satellite altimeter and scatterometer wind speed algorithms for nadir cross-section data compared to the present aircraft mss results and *Cox and Munk* [1954] optical data according to *Wu* [1972]. MCW is the modified Chelton-Wentz algorithm [*Witter and Chelton*, 1991]; BROWN is the *Brown et al.* [1981] algorithm without second-stage wind speed polynomial smoothing; ROWS is the present aircraft result; and SASS is the SASS I scatterometer nadir wind speed algorithm for horizontal polarization [*Schroeder et al.*, 1984]. Wind speed is neutral equivalent in the case of the ROWS and SASS I data, uncorrected 10-m level wind speed otherwise.

et al. [1987] which Dobson et al. show provides a somewhat better fit to the Geosat Exact Repeat Mission (ERM) data. This algorithm is compared to the present aircraft results and Geosat data by *Jackson* [1988], where also one may find a comparison of the present results with the Chelton-Wentz algorithm, the antecedent to the MCW algorithm.

Figure 11 shows Geosat ERM cross-section data (E. Dobson, personal communication, 1991) converted to mss values according to (13) (with $\rho_n' \equiv 0.37$) compared to the ROWS results (8) and (14) and linear and fifth-degree polynomial regression fits to the data. The linear regression on the Geosat ERM data gives a result almost identical to the ROWS results, namely, $m_n^2 = 0.0024\ U_{10} + 0.012$. The polynomial fit suggests by its inflections the basic structure contained in the *Brown et al.* [1981] algorithm. Particularly, the fit exhibits a logarithmic sort of behavior at low wind speeds, linear behavior at moderate wind speeds, and an enhanced wind response at highest wind speeds (albeit some several meters per second above the 11 m s^{-1} jump point in the Brown et al. curve). Comparison with Figure 10 shows that this polynomial fit is virtually identical to the MCW curve for all $U_{10} < 15$ m s^{-1}. (Note that the MCW curve is almost identical to the Brown et al. curve shown in Figure 10 for winds <7 m s^{-1}, so that both algorithms agree well with the ERM data in this range. Such agreement is not found in the case of the two-stage *Brown et al.* [1981] algorithm; see below).

Figure 12 from *Ebuchi et al.* [1992] shows Geosat ERM data from the Sea of Japan in the form of a scatterplot of Geosat winds inferred according to the (two-stage) *Brown et al.* [1981] algorithm versus buoy-observed winds. The Ebuchi et al. raw data being unavailable to us, we have therefore plotted the ROWS result (14) in the function space of this scatterplot. The resultant curve evidently represents the Ebuchi et al. data better over most wind speeds, particularly above the 11 m s^{-1} branch point in the Brown et al. algorithm. At low wind speeds, $U_{10} < 7$ m s^{-1}, it is seen from Figure 12 that the one-stage Brown et al. algorithm given by (15) below provides a better fit than either the ROWS result or the two-stage Brown et al. algorithm.

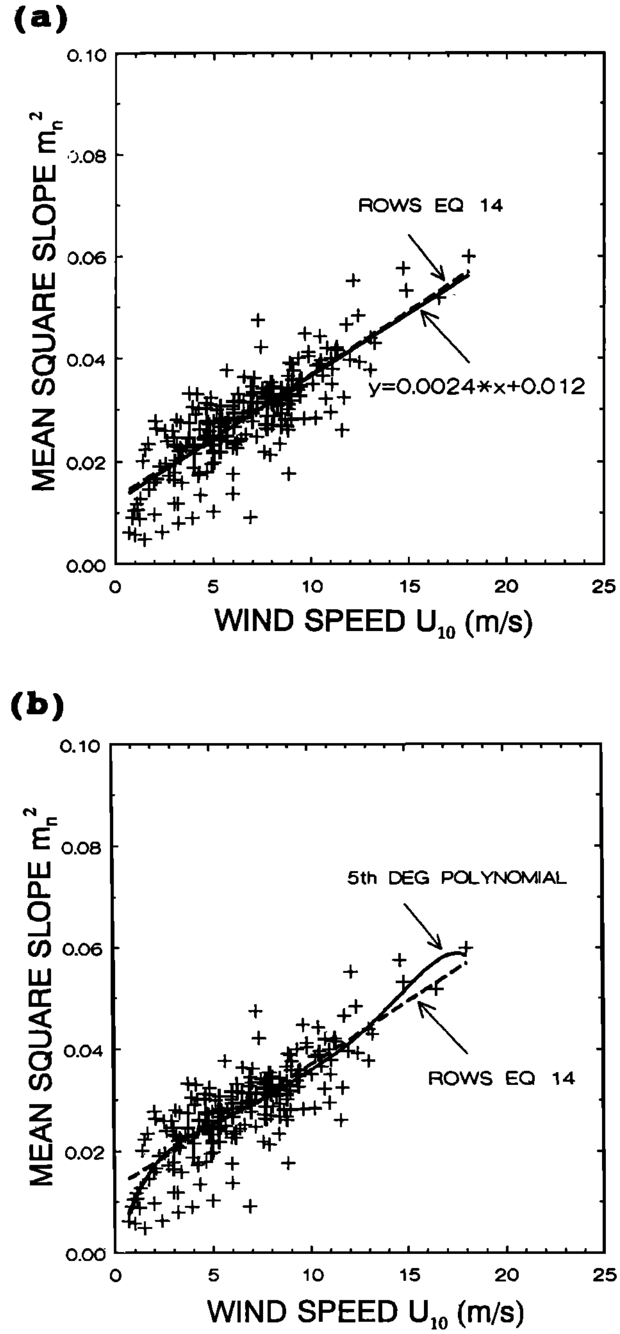

Fig. 11. Inferred mss from Geosat ERM data (courtesy of E. Dobson, Johns Hopkins University Applied Physics Laboratory) compared to aircraft ROWS result with (*a*) linear regression on the ERM data and (*b*) fifth-degree polynomial fit to the data.

One must be careful not to attach too much significance to

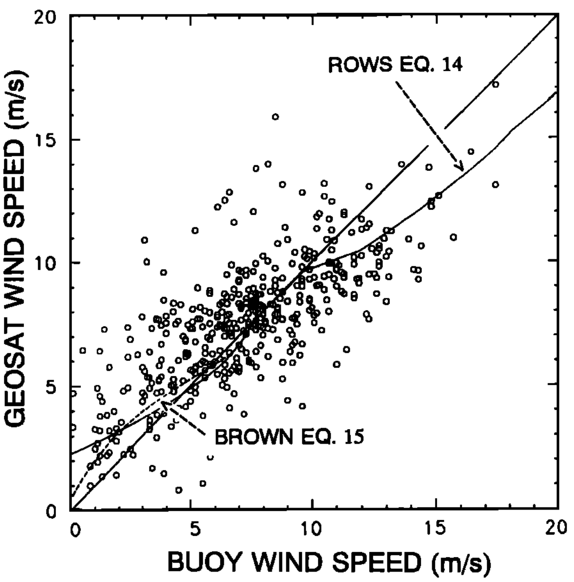

Fig. 12. Geosat data, from Figure 2*b* of *Ebuchi et al.* [1992], shown as a scatterplot in the function space of the *Brown et al.* [1981] two-stage wind speed algorithm (equal to Geosat wind speed). The present aircraft result, equation (14), is traced in this function space (solid curve); also the low wind speed branch of the Brown et al. algorithm without polynomial smoothing given by (15) (dashed curve).

these results, particularly at the high wind speeds. First, very few data points exist at the higher wind speeds in either satellite or aircraft data sets (none above 15 m s^{-1} in the aircraft data except for the *Jones et al.* [1977] point; two points in the *Dobson et al.* [1987] ERM data of Figure 11; four in the *Ebuchi et al.* [1992] data); second, the ROWS error bounds at high wind speeds are sizeable (Figure 4); third, unaccounted for stability effects in the satellite altimeter data and wind speed algorithms, while generally small at high wind speeds, may be responsible for some of the differences between the curves in Figure 10. For example, the 14°C air-sea temperature difference on January 18, 1983, in MASEX resulted in a difference of 0.8 m s^{-1} between the actual and equivalent neutral 10-m wind speeds, which, while not great, is enough to move the ROWS datum over to the upper branch of the *Brown et al.* [1981] curve in Figure 10. One should also note that inordinate variability and possibly bias can be introduced if a data set contains large departures from equilibrium wind/wave conditions. Particularly, a large number of falling wind events in any particular data set could bias the mss versus local wind on the high side because of the inertia contained in the longer-wave components. This alone could explain the relatively higher mss values seen in the Dobson et al. Geosat data and in the original Geos-3 altimeter data set of *Brown et al.* [1981] at high wind speeds compared to the present data and the Ebuchi et al. data, since the Dobson et al. and Brown et al. data were obtained essentially at random with respect to the meteorology, while the data in the latter two cases were obtained during relatively steady wind conditions during cold air outbreak episodes (in the case of the ROWS data during MASEX; cf. Table 1).

4.3. *Optical Data*

Cox and Munk's [1954] clean surface mss data were shown by *Wu* [1972] to be well fitted by a logarithmic function below 7 m s^{-1} that is practically the same as the low wind speed branch of the Brown et al. curve in Figure 10, which is given by

$$m_n^2 = 0.010\ (\ln U_{10} + 1.1) \tag{15}$$

Above 7 m s^{-1} Wu gives for the optical mss

$$m_f^2(U;\ \infty) = 0.10\ (0.85\ \ln U_{10} - 1.45) \tag{16}$$

The result is plotted in Figures 10 and 14 along with the microwave results. The Cox and Munk linear regression for all wind speeds on the other hand is given by

$$m_f^2(U;\ \infty) = 0.051 U_{10} + 0.003 \tag{17}$$

The result is plotted in Figures 4 and 14. If Cox and Munk's wind data are converted to u_* by the profile method, assuming neutral stability, then a linear regression on u_* gives

$$m_f^2(U;\ \infty) = 0.042 u_* + 0.020 \tag{18}$$

The result is plotted in Figure 4. Comparing this result to the K_u-band result (9), we see that the two curves intersect at $u_* = 0.21$ m s^{-1} or around 6 m s^{-1} wind speed. This is close to Wu's breakpoint of 7 m s^{-1} and to *Munk*'s [1947] postulated "critical" wind speed marking the transition from smooth to rough flow in the boundary layer. Wu associates this transition with the rapid growth of capillary waves around this wind speed, but it may also be related to incipient air flow separation from the short gravity wave crests and wave breaking [*Csanady*, 1985; *Donelan*, 1990].

While *Wentz* [1976] suggests that these optical data might be biased low, the measurements of *Haimbach and Wu* [1985] and *Hwang and Shemdin* [1988] do not support this view; thus we may assume for the present that these data are basically correct. Assuming this is the case, it would follow then from the near equality of the microwave and optical results below 7 m s^{-1} wind speed that there is relatively little slope variance contained in the capillary range at low wind speeds, consistent with Wu's hypothesis. Numerous Bragg scatter observations [e.g., *Schroeder et al.*, 1985; *Donelan and Pierson*, 1987] as well as direct laboratory measurements [*Jähne and Riemer*, 1990] support this view in that they show a very rapid capillary wave growth (or at least growth of small-scale surface structures) around 5–7 m s^{-1}. Above 10 m s^{-1}, comparison of (8) and (17) shows that the K_u-band data are some 30–40% lower than the clean surface optical data, which is again consistent with *Wu*'s [1972] hypothesis. The Cox and Munk slick surface data represent the mss of waves longer than 0.5 m or so. These mss data will be seen to be consistent with the spectrum model developed in section 6.

4.4. *Other Evidence*

Wilheit [1979] used multifrequency, passive microwave data and a GO scattering model to infer an mss wind speed dependence that accords with the present observations. In particular, he infers an mss at 14 GHz that is about 60% of the Cox and Munk mss, in agreement with the above results.

Jackson et al. [1985] inferred mss values indirectly from modulation transfer function (MTF) modulus measurements in the ROWS instrument "wave spectrometer" mode that are in good agreement with the present observations. For wind speeds between 5 and 18 m s^{-1}, Jackson et al. find $m_g^2 = 0.0028U + 0.009$. *Plant*'s [1982] limit on the mss inferred from observed growth rates of waves primarily in the gravity wave range is consistent with the present data. Assuming an anisotropy ratio of $r^2 = 0.85$ appropriate to the gravity wave portion of the spectrum (Appendix A), Plant's limit on the mss becomes, for example, for an air and water temperature of 0°C,

$$m_f^2(U;\ 500\ \mathrm{m}^{-1}) \leq 0.08 \pm 0.04 \tag{19}$$

(i.e., for waves longer than about 1.2 cm). The raw K_u-band data are seen to remain below the nominal limit of 0.08 for winds exceeding 20 m s^{-1}, while the optical data reach the Plant limit around 15 m s^{-1}. While the K_u-band data cannot be directly compared to the Plant limit because of the different cutoff wavelengths, yet a comparison is not entirely invalid, since the diffraction contribution to the apparent mss at high wind speeds is seen to be roughly equal to the additional slope variance contained between the diffraction limit of order of 0.1 m and Plant's cutoff wavelength of order of 0.01 m according to the model calculations of section 6. Assuming the two quantities are comparable, it then follows that the microwave data are consistent with an approach to the nominal Plant limit at high wind speeds. If the Plant limit is indeed correct, then this would lead one to infer that form drag exerted by (principally short) gravity waves is supporting the bulk of the wind stress at high wind speeds as suggested by *Csanady* [1985] and *Donelan* [1990].

5. Implications for the Equilibrium Range

The mss data can be used to help resolve a present controversy over the form of the so-called equilibrium range of the surface gravity wave energy spectrum. *Phillips* [1985] argues that his classical, universal form of the equilibrium range spectrum is no longer tenable; that instead of the nondirectional height spectrum, $\bar{F} \equiv \int F(\mathbf{k})k\,d\phi$, being of the form

$$\bar{F}(k) = Bk^{-3} \tag{20}$$

it should be of the form

$$\bar{F}(k) = A_u(U/g^{1/2})k^{-5/2} \tag{21}$$

or, to be more precise, of the same form as (21), but with the wind dependence given in terms of u_*. If the spectrum is nearly fully developed, this form is close to the peak-scaled form,

$$\bar{F}(k) = A'\tilde{k}^{1/2}k^{-3} \tag{22}$$

where $\tilde{k} = k/k_o$ where the peak wave number, $k_o \sim g/U^2$. According to Phillips the equilibrium range form (22) should extend from wavenumbers near k_o to wavenumbers approaching $k = g/u_*^2$. Although this form of the equilibrium wave spectrum is universally supported by observations in the rear-face region of the spectrum, it cannot extend to the very high wavenumbers that Phillips supposes without seriously violating the constraints on the spectrum imposed by the slope data. To see this, let $A_u = 0.002$, which is a nominal value approximating the consensus of (mostly frequency domain) field observations in the range $2 \leqslant \tilde{k} \leqslant 10$ [see *Phillips*, 1985, Tables 1; *Battjes*, 1987, Table 2], and let $u_* = (1/30)\ U$ and $k_o = g/U^2$. Then according to (21) or (22), the mss representing most all of the gravity wave range of the spectrum is no less than

$$m_f^2 = \int_{g/U^2}^{900g/U^2} k^2\bar{F}(k)\ dk \approx 60A_u = 0.12 \tag{23}$$

provided $g/u_*^2 \ll k_c$ where $k_c \sim 360$ m^{-1} is the wavenumber of the gravity-capillary wave phase speed minimum. This value of the mss, ostensibly representing the slope variance of gravity waves alone, is of the order of the optical mss at the higher wind speeds and is considerably higher than the observed microwave mss m_g^2 which, we note, is already inflated relative to the true mss in $k \leqslant g/u_*^2$ since it also includes the slope variance in $g/u_*^2 \leqslant k \leqslant k_d = O(100\ \mathrm{m}^{-1})$ as well as yet an unaccounted for diffuse diffraction component (see section 6). Since this value is equal to the upper error bound on Plant's limit (19), this would imply that the gravity waves alone are supporting all of the wind stress. Indeed, as *Phillips* [1985] remarks, if the form (21) truly applies to wavenumbers as high as g/u_*^2, then there is virtually no allowance for gravity-capillary wave slope variance. *Kitaigorodskii* [1983] (hereafter referred to as *K*) on the other hand, argues for the existence of two subranges in the equilibrium wavenumber spectrum of gravity waves. In the first subrange, $2 \leqslant \tilde{k} \leqslant 10$, the integrated, nondirectional spectrum is supposed to have the rear face form (21); while, in the second subrange, $10 \leqslant \tilde{k} \leqslant (U/u_*)^2 \approx 900$, it is supposed to be of the classical Phillips form (20). K's theoretical arguments are supported by numerous frequency domain observations which show, in addition to the well-established f^{-4} ($k^{-5/2}$) behavior in the rear-face region, a fairly abrupt change of spectral slope around $f = 3f_o$ (or $\tilde{k} = 9$) to something like the f^{-5} (k^{-3}) law. In addition to those observations cited by K, one may also cite the (frequency domain) observations of *Leykin and Rozenberg* [1984], *Liu* [1989], and *Kwaii et al.* [1977] as supporting his hypothesis. (Note that the spectral slope changes are not clearly evident in all the Kwaii et al. data, wherefore one may mistakenly underestimate A_u by assuming the rear-face f^{-4} range to extend to much higher frequencies than it actually does [cf. *Phillips*, 1985, p. 518]). In the wavenumber domain, besides the single stereo spectrum example cited by K, one may point to the Bragg scatter data of *Daley* [1973], particularly the *P* band (75 cm) wavelength data, as providing yet further evidence for a Phillips saturated range in the high-frequency range for which $k < g/u_*^2$. The mss data, both the microwave and the optical slick and clean surface data, provide rather conclusive evidence in support of K's view.

Consider the peak-scaled, rear face form (22). Let $k_o = g/U^2$, so that $A' = A_u$. Denote the breakpoint wavenumber between the rear face and Phillips subrange by k_1 and let $\tilde{k}_1 = k_1/k_o$. If one assumes that at the higher wind speeds, the spectrum in the range $g/u_*^2 \leqslant k \leqslant k_d = O(100\ \mathrm{m}^{-1})$ is no less saturated than the spectrum in the Phillips subrange for which $k < g/u_*^2$ is follows that the mss is, at least,

$$m_f^2 = 2A_u(\tilde{k}_1^{1/2} - 1) + B\ \ln\ (k_dU^2/g\tilde{k}_1) \tag{24}$$

With nominal values of $A_u = 0.002$, $\bar{k}_1 = 9$ (implies $B = 3A_u = 0.006$ by continuity at k_1) and $k_d = 80\ \mathrm{m}^{-1}$, (24) becomes

$$m_f^2(U;\ 80\ \mathrm{m}^{-1}) = 0.012(\ln U + 0.62) \qquad (25)$$

which is a weaker wind response than observed in the raw ROWS mss m_g^2 and satellite mss m_n^2 at the higher wind speeds, but a greater one than observed in the reanalyzed, shape-based RADSCAT data, as seen in Figure 9.

The physics governing the form of the spectrum of gravity waves in the so-called equilibrium range is still not entirely understood, despite the important contributions of *Kitaigorodskii* [1983] and *Phillips* [1985]. *Banner* [1990] has provided new insight into the problem by elucidating the relationship of wave directionality to the form of the equilibrium range spectrum. In particular, he shows how an increasing directional spreading with wavenumber in the rear face region of the spectrum (i.e., the high wavenumber side of the spectral peak) can result in nondirectional spectrum exhibiting $-5/2$ power law behavior even though in the along-wind direction the directional spectrum may exhibit a classical Phillips -4 power law over the entire gravity wave range. As the spreading approaches saturation, that is, becomes nearly isotropic (cf. Appendix A), the $-5/2$ power law for the nondirectional spectrum then transitions to the -3 power law, in accordance with the model behavior discussed above.

The ultrahigh frequency gravity wave range, $g/u_*^2 \leqslant k \leqslant k_d$, say, is known to be wind speed dependent from Bragg scatter observations at L and C bands [*Daley*, 1973; *Thompson and Weissman*, 1983; *Durden and Vesecky*, 1985], as is the gravity-capillary range from X- and K_u-band observations. As an ad hoc model of the wavenumber spectrum in the ultragravity and gravity-capillary ranges, we assume the Bragg scatter-constrained spectrum model of *Durden and Vesecky* [1985]. If we assume that the diffraction component of σ^o_{DIF} in the case of the azimuthally integrated cross section is relatively insensitive to capillary wave directionality, then we may adopt the Durden and Vesecky form of the nondirectional spectrum given by

$$F(k) = Bk^{-3}(bku_*^2/g_*)^{a\ \ln(k/2)}, \qquad k \geq 2\ \mathrm{m}^{-1} \qquad (26)$$

where B is the Phillips constant, as before, $g_* = g + \gamma k^2$ ($\gamma = 7.25 \times 10^{-5}\ \mathrm{m}^3\ \mathrm{s}^{-2}$), and where a and b are empirically determined, dimensionless constants having the values, $a = 0.225$ and $b = 1.25$. The onset of this range, $k = 2\ \mathrm{m}^{-1}$, is somewhat arbitrary, but it is consistent with the requirement that this range include all $k > g/u_*^2$, which it does for all practical values of u_*.

6. Model Results

The above equilibrium spectrum model is used along with the perfect conductivity two-scale cross section model described in section 2 and Appendix B to analyze the mss results, assuming, as in the above, that $k_o = g/U^2$ and $\bar{k}_1 = 9$. For simplicity, in the spectrum model (26), let $u_* = (1/30)U$. (Considering the preliminary and primarily illustrative nature of the calculations, it is not really appropriate to use at this point a more representative wind speed dependent drag coefficient; such refinements should await for example a better understanding of the proper wind scaling of the first equilibrium subrange and a proper parameterization of wave age effects [e.g., *Janssen et al.*, 1989]). The model is then run for $k_d = 60$, 80, 100, and $200\ \mathrm{m}^{-1}$ and $B = 3A_u = 0.004$, 0.005, and 0.006.

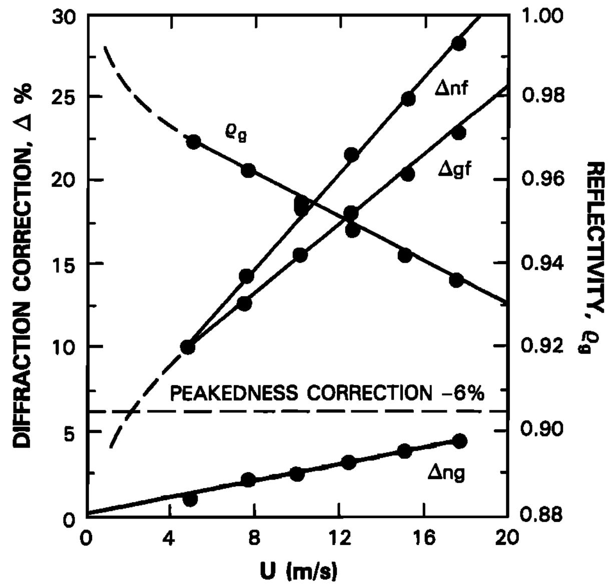

Fig. 13. Various diffraction and peakedness corrections, as defined in the text, as a function of wind speed.

Given the computed $\sigma^o_{2\mathrm{S}}$ as a function of wind speed, we now least squares fit the GO form (2) to it in order to determine a trial relationship between m_g and m_f. Letting $A = \rho_g^*/m_g^2$ in (2) (the asterisk denotes the perfect conductivity case), we solve $\partial I/\partial A = 0$ and $\partial I/\partial m_g^2 = 0$ simultaneously, where

$$I = \int_0^{3m^2} [\sigma^o_{\mathrm{GOG}}(\theta) - \sigma^o_{2\mathrm{S}}(\theta)]^2\ d(\tan^2\theta) \qquad (27)$$

In addition to generating a table of m_g^2 versus m_f^2, the two-scale model is also used to generate ersatz constant reflectivity ($\rho_n^* \equiv 1$) m_n^2 data according to the relationship

$$m_n^2 \equiv 1/\sigma^o_{2\mathrm{S}}(0°) \approx m_g^2/\rho_g^* \qquad (28)$$

The results are shown graphically in Figure 13 for the case $A_u = 0.002$ ($B = 0.006$) and $k_d = 80\ \mathrm{m}^{-1}$ as the relative differences, $\Delta_{gf} \equiv (m_g^2 - m_f^2)/m_f^2$ and $\Delta_{ng} \equiv (m_n^2 - m_g^2)/m_g^2$ ($\approx 1/\rho_g^* - 1$). Both of these differences are approximately linearly increasing functions of wind speed. Over the range $U = 5$–$20\ \mathrm{m\ s}^{-1}$, Δ_{gf} ranges from 10 to 26% while Δ_{ng} ranges from 4 to 7% and ρ_g^* varies from 0.97 to 0.93. The reduction in ρ_g^* from the perfect conductivity Fresnel value of 1, we note, is much less than the comparable reduction in ρ_f over the same wind speed range (cf. Appendix B) for the apparent reason that power diffracted away from the specular direction at any filtered surface specular point is largely compensated for by power diffracted back into that direction from other nonspecularly oriented facets.

The model results for $m_f^2(U;\ k_d = 80\ \mathrm{m}^{-1})$, $m_g^2(U;\ k_d = 80\ \mathrm{m}^{-1})$, (with peakedness correction) and $m_f^2(U;\ k_d = 200\ \mathrm{m}^{-1})$ are compared to the aircraft observations in Figure 14, where $m_f^2(U;\ 200\ \mathrm{m}^{-1})$ is chosen to correspond to Wentz' m_f^2 data for which $k_d = 193\ \mathrm{m}^{-1}$ is an average value (Table

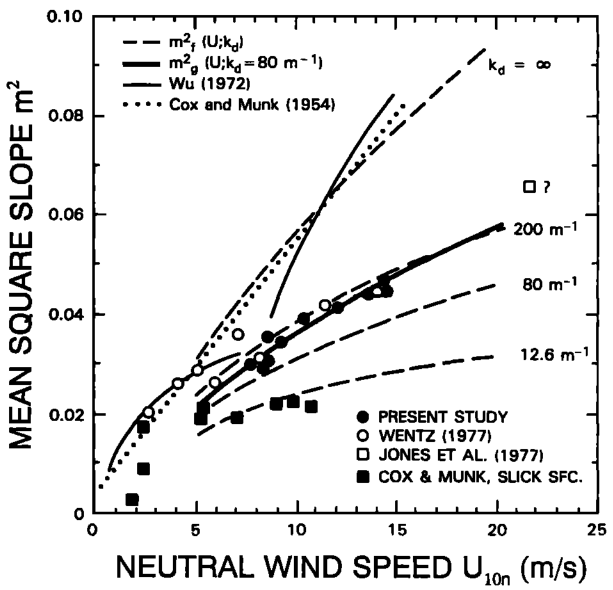

Fig. 14. Model predictions of filtered surface m_f^2 and "gross fit" K_u-band mss m_g^2 versus wind speed for various diffraction limit wavenumbers k_d compared to microwave and optical slick surface data and to *Cox and Munk*'s [1954] linear and *Wu*'s [1972] logarithmic fits to the optical clean surface data.

2). The model results for $m_g^2(U;\ 80\ \text{m}^{-1})$ are in excellent agreement with the ROWS m_g^2 results over all wind speeds; they are also close to the model $m_f^2(U;\ 200\ \text{m}^{-1})$ and Wentz results. Thus combining the ROWS and Wentz data as in Figure 4 is seen to have some justification.

The model result for Δ_{ng} shown in Figure 13 is used to facilitate the comparison between the aircraft shape-based data and the satellite nadir data, namely, according to (14). Although the correction is small (and of questionable significance), it tends to bring the aircraft results into closer agreement with the satellite results, particularly the MCW results at intermediate wind speeds.

An integration of the model spectrum over all wavenumbers yields the total surface slope variance $m_f^2(U;\ \infty)$; its mss is also plotted in Figure 14. This mss result is almost identical to the *Cox and Munk* [1954] clean surface linear regression result (17), also plotted in Figure 14. However, the model fails to exhibit the behavior around the critical wind speed suggested by *Wu*'s [1972] analysis. This is not surprising as (26) contains no viscosity, only surface tension and gravity parameters. Integrated to 0.5 m wavelength (k_d = 12.6 m^{-1}), the model also produces an mss in accord with Cox and Munk's slick surface observations, as seen in Figure 14.

7. CONCLUSION

While some significant discrepancies between data sets exist which need to be resolved, nevertheless, a fairly clear and consistent picture of the behavior of the sea surface mean square slope (mss) wind response emerges from an examination of the optical and microwave data presented herein. Once adjusted as to level according to the new shape-based mss data presented here, all K_u-band frequency (~2-cm wavelength) inferred mss data are seen to be bracketed in the extremes by the *Brown et al.* [1981] altimeter algorithm data (on the high side) and the reanalyzed RADSCAT [*Schroeder et al.*, 1984] and *Masuko et al.* [1986] *X* band data (on the low side), while the SASS I, *Wentz* [1977], the modified Chelton-Wentz (MCW) of *Witter and Chelton* [1991] and the present data occupy a middle ground in terms of wind speed response. Examination of Geosat data from the Exact Repeat Mission [*Witter and Chelton*, 1991; also E. Dobson, personal communication, 1991] and from *Ebuchi et al.* [1992] indicates that the mss from the MCW algorithm and the present mss results are perhaps most representative of the mss response over the largest range of wind speeds.

At low wind speeds, $U \leqslant 7$ m s^{-1}, the K_u-band and optically measured (clean surface) mss are virtually identical. In this range the mss appears to be well approximated by the mss inferred from either the one-stage Brown et al. or the MCW wind-speed algorithm (cf. equation (15)). Above the "critical" wind speed of 7 m s^{-1} the regression results (8) and (14) from the present aircraft measurements appear to well represent the behavior of the K_u-band diffraction effective mss. These results may be immediately applied to scattering studies based on a Gaussian slope distribution, but if a more realistic, non-Gaussian distribution is used, the mss values should be raised upward by approximately 6% to account for unmodeled peakedness.

An analysis of diffraction has indicated that the raw slope data may be interpreted in the context of a two-scale model with a scale separation wavelength of the order of 3–6 electromagnetic wavelengths, or about 10 cm for K_u band, in basic agreement with previous estimates by *Brown* [1978] and *Durden and Vesecky* [1985], for example. For the perfect conductivity case to which we have confined ourselves here, diffraction from the small-scale structure beyond the diffraction limit may account for as much as 20% of the raw or apparent slope signal. Future work should extend the present results to the finite conductivity case.

This study supports *Kitaigorodskii*'s [1983] view of the equilibrium range of the spectrum of gravity waves. Particularly, we find that in order not to violate the constraints on the spectrum imposed by the mss data, the $k^{-5/2}$ wind speed dependent form of the nondirectional height spectrum observed in the rear-face region of the spectrum must transition to something more like the classical Phillips' k^{-3} power law at wavenumbers around 10 times the peak wavenumber. Whatever the underlying physics [*Kitaigorodskii*, 1983; *Phillips*, 1985], this behavior appears to be related to the directional spreading characteristics as a function of wavenumber as discussed by *Banner* [1990].

A simple model of the wavenumber spectrum of the sea surface for nearly fully developed conditions consisting of the above equilibrium range model for the gravity waves plus a Bragg scatter-constrained model of the gravity capillary range after *Durden and Vesecky* [1985] produced mss values consistent with (many) microwave and optical (clean and slick surface) mss observations. This model therefore is likely to embody correctly the gross aspects of the (slope) spectral behavior versus wind speed for nearly fully developed conditions.

The *Hammond et al.* [1977] broad-beam altimeter technique adopted in this study is an efficient way of making relative near-nadir cross-section and wave-height measurements simultaneously. A statistically stable diffraction effective mean square slope parameter can be derived from the waveform trailing edge with as little as 10-s integration time.

The technique is insensitive to typical aircraft attitude variations, does not require absolute power calibration, and consequently, the data processing is relatively simple. In the future, mss data such as may be obtained according to this technique may be particularly valuable when they are combined with other remotely sensed surface and boundary layer data. For example, the directional spectrum of the energy-containing waves can now be measured remotely using sensors such as surface contour radar [*Walsh et al.*, 1985] or the ROWS (radar ocean wave spectrometer) in its spectrometer mode [*Jackson et al.*, 1985] and the gravity-capillary wave portion of the spectrum estimated from large-angle Bragg scatter measurements. Combining such surface data with appropriate boundary layer data should enable one to develop a rather complete picture of the surface and its role in mediating fluxes across the air-sea interface in the variety of conditions found in nature.

Appendix A: Slope Distribution Anisotropy

The GO approximation to the cross section in the case of an anisotropic, Gaussian sea surface is

$$\sigma^o_{GO} = \rho(\sec^4\theta/2m_1m_2) \cdot \exp\left[-(1/2)\tan^2\theta\,(\cos^2\phi/m_1^2 + \sin^2\phi/m_2^2)\right] \quad \text{(A1)}$$

where m_1^2 and m_2^2 are the principal mss components and ϕ is the direction relative to the direction of the major axis (nominally, the wind direction). *Wentz'* [1977] analysis of the K_u-band RADSCAT data gives an average value of the aspect ratio $r^2 = m_2^2/m_1^2 = 0.88$. Analysis of the ROWS spectrometer mode average backscattered power data via a two-dimensional model fit using (A1) yields for the fetch-limited conditions observed in the MASEX experiment an average $r^2 = 0.83 \pm 0.008$ (Figure 15 is an example of a model fit), while ROWS data for confused sea and low and variable wind conditions show an r^2 approaching unity [cf. *Jackson*, 1991, Table 2]. The *Schroeder et al.* [1984] data give for an average of ten cases $r^2 = 0.82$. The K_u-band observed anisotropy is thus comparable to *Cox and Munk*'s [1954] slick surface data, which average to $r^2 = 0.86$. Their clean surface data on the other hand give an average $r^2 = 0.75$, which is consistent with a gravity-capillary range contribution to the mss which is more strongly directional than the high-frequency gravity wave range contribution. On the basis of the mss data as well as other data (e.g., the L band Bragg scatter data of *Thompson et al.*, 1983], one may conclude that the short gravity waves are nearly isotropic, consistent with the physical picture drawn by *Csanady* [1985].

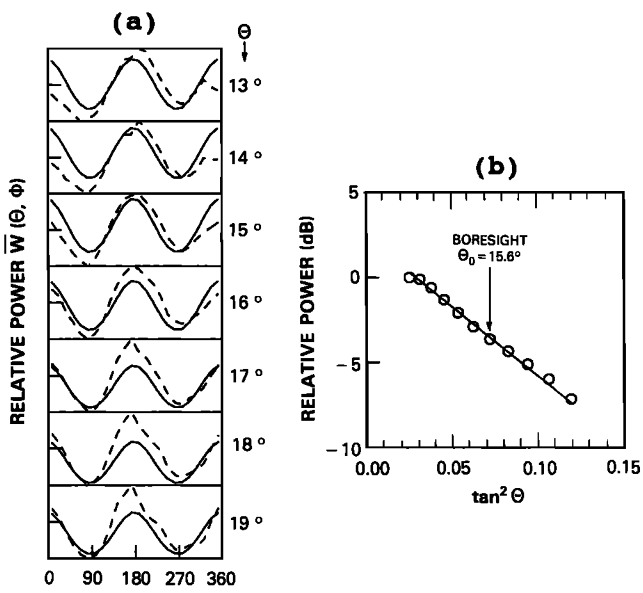

Fig. 15. Two-dimensional, Gaussian surface, GO scattering model fit to quasi-specular backscatter data obtained from the ROWS operating in its rotating antenna spectrometer mode during MASEX in fetch-limited conditions shown (*a*) as a function of azimuth for various incidence angles and (*b*) in azimuthally integrated form as a function of tangent squared of the incidence angle after removal of beam pattern of the rotating antenna. The first harmonic has been removed. Data from January 16 flight tape/file 3/2, measured mss axial ratio $r^2 = 0.80$, mss $m_g^2 = 0.055$, assuming a 10° beamwidth. This mss retrieval is biased with respect to the altimeter mode measured mss of 0.046 nearby.

Appendix B: Two-Scale Approximation to the Physical Optics Integral

The physical optics (PO) or Kirchhoff integral formulation [*Beckmann and Spizzichino*, 1963] provides a paradigm of near-nadir, quasi-specular backscatter in that it can be shown, at least in the perfect conductivity case, to contain both geometrical optics (GO) and small perturbation (SP) results as limiting forms, in the latter case asymptotically as $\theta \to 0$. It thus may serve as a basis for an analysis of diffraction effects in quasi-specular backscatter. Particularly, it may be used to establish objectively a scale separation wavenumber when decomposing the backscatter into quasi-specular and diffuse diffraction contributions according to a two-scale model [see *Thompson*, 1988].

Numerically, *Chen and Fung* [1988] have shown that the PO integral is more robust than generally has been supposed in terms of its domain of validity in surface height, slope, and correlation length scale. Analytically, *Jackson* [1972], *Holliday* [1987], and *Rodriguez* [1991] provide further evidence of this, particularly vis a vis its correspondence with SP. *Jackson* [1972] and *Rodriguez* [1991] derived local surface curvature corrections to the Kirchhoff tangent-plane field boundary values from the magnetic field integral equation (MFIE) of the order of $(4k_{em}r_c \cos^3\theta)^{-1}$ × (Kirchhoff value), where r_c is the radius of curvature, and showed how these corrections produce an angular and polarization cross-section dependence near vertical incidence that asymptotically agrees with SP. *Jackson* [1972], for example, finds vertical (denoted by plus signs) and horizontal (denoted by minus signs) polarization backscatter cross sections that in the small roughness-height limit reduce to the SP form $\sigma^o_\pm = 16\pi k^4 g_\pm(\theta)F(2k_{em}\sin\theta, 0)$ where $F(\mathbf{k})$ is the height spectrum and where $g_\pm(\theta) \sim 1 \pm 2\tan^2\theta$. For small θ, this result patently agrees with the classic SP result according to which $g_\pm(\theta) = [1 \pm \sin\theta]^2$ [*Valenzuela*, 1978; *Brown*, 1978]. These curvature-corrected, or "extended", Kirchhoff results demonstrate that it is no mere accident that PO and SP results agree near nadir, as successive higher-order local approximation to the field boundary values does indeed consistently generate the proper angular and polarization dependence of the scattering under SP conditions. Thus it is safe to say that in the case of near-nadir backscatter, extended PO, if not PO itself, subsumes SP and that therefore it contains conventional two-scale model results [e.g., *Brown*, 1978]. For large angles of incidence, successive local approximation may fail, but the correspondence between PO and SP may be established in this case as well, as done by *Holliday* [1987], also using the MFIE.

The ability of PO (or extended PO) to reproduce SP results near nadir may perhaps be appreciated more fully if we examine the small curvature condition for the validity of PO alone, which, according to the above, can be expressed as $4k_{\mathrm{em}}r_c \cos^3\theta \gg 1$. Allowing even a very large 10:1 inequality, it is evident that (for θ not too large) the radius of curvature can be as small as one em wavelength. For typical short wave slopes $ak = 0.2$–0.4 (a being the amplitude and k being the wavenumber) it follows that a comparable horizontal length scale of the order of one em wavelength is permissible as well. In practice, even smaller-length scales may be tolerated, particularly, as the polarization effects arising from the finite surface curvature are small near nadir (essentially zero at nadir for a quasi-isotropic surface in accord with the classic result for diffraction from a paraboloid of revolution). As polarization state has in fact no sensible effect on the results of the analyses contained herein (as we have demonstrated by actual fitting of the GO and two-scale models to the extended PO-like polarization cross-sections in the isotropic, finite roughness height case), we elect here to develop the two-scale model approximation from the conventional PO integral, rather than extended PO, in order to simplify the exposition.

The PO integral for the far-zone backscatter cross section of a perfectly conducting sea surface $z = h(x)$ can be written as

$$\sigma^o_{\mathrm{PO}} = \pi \sec^4\theta\beta^2 \int \langle \exp(i\beta\Delta h)\rangle \cdot \exp(-i\beta\mathbf{s}\cdot\Delta\mathbf{x})\, d\Delta\mathbf{x}/(2\pi)^2 \qquad \text{(B1)}$$

where $\beta = 2k_{\mathrm{em}}\cos\theta$, $\langle\cdots\rangle$ denotes ensemble average; Δh and the $\Delta\mathbf{x}$ are the height difference and horizontal separation vector between two points on the surface, respectively, where $\mathbf{s} = \tan\theta(\cos\phi, \sin\phi)$ is the specular slope vector, ϕ being the azimuth angle. Assuming that the surface can be spectrally decomposed into statistically independent large- and small-scale components h_f and h_s, respectively, such that h_f is planar of the order of a few em wavelengths and h_s is Rayleigh smooth, $\beta^2\langle h_s^2\rangle \ll 1$, then on expanding the height difference as $\Delta h = \nabla h_f \cdot \Delta\mathbf{x} + \Delta h_s$, it follows from (B1) that the cross section can be expressed as $\sigma^o_{\mathrm{PO}} \approx \sigma^o_{2S} = \sigma^o_{\mathrm{GOF}} + \sigma^o_{\mathrm{DIF}}$ where

$$\sigma^o_{\mathrm{GOF}} = \rho_f^* \pi \sec^4\theta p_f(\mathbf{s}) \qquad \text{(B2)}$$

[e.g., *Barrick*, 1968] where p_f is the large-scale surface slope pdf, $\rho_f^* = 1 - \beta^2\langle h_s^2\rangle$ is a reduced reflectivity (the asterisk denoting the perfect conductivity case) and where

$$\sigma^o_{\mathrm{DIF}} = \pi \sec^4\theta\beta^2 \int_{-\infty}^{\infty}\int_{-\infty}^{\infty} H(|\mathbf{k}| - k_d)F(\mathbf{k})p_f(\mathbf{s} - \mathbf{k}/\beta)\, d\mathbf{k} \qquad \text{(B3)}$$

where H is an arbitrary high-pass filter, k_d being the scale separation wavenumber, and F is the surface height spectrum. For a Gaussian, isotropic surface, $p_f = (1/\pi m_f^2)\exp(-s^2/m_f^2)$, where $s = |\mathbf{s}|$ and $m_f^2 \equiv \langle(\nabla h_f)^2\rangle$, and the diffuse term can be expressed, assuming H is the Heavyside function, as

$$\sigma^o_{\mathrm{DIF}} = (\sigma^o_{\mathrm{GOF}}/\rho_f^*)\beta^2 \int_{k_d}^{\infty} \bar{F}(k)\exp[-(k/\beta m_f)^2] I_o(2ks/\beta m_f^2)\, dk \qquad \text{(B4)}$$

where I_o is Bessel's function and $\bar{F}(k)$ is the nondirectional height spectrum, $k = |\mathbf{k}|$. For the computations, $\bar{F}(k)$ is given by (26) in the text. In the Gaussian, isotropic surface case the parent PO integral (B1) reduces to the well-known form

$$\sigma^o_{\mathrm{PO}} = (\beta^2 \sec^4\theta/2)\int_o^{\infty} \exp[-\beta^2 D(r)/2]\, J_o(\beta s r) r\, dr \qquad \text{(B5)}$$

where $D(r) = \langle(\Delta h)^2\rangle$ is the structure function and J_o is Bessel's function. For a Phillips spectrum $\bar{F} = B\, k^{-3}$, $k \geq k_o$ and zero otherwise, a rational approximation to $D(r)$ near the origin is [*Luke*, 1966] $D(r) \sim (Br^2/2)\,[1 - \gamma - \ln(k_o r/2)]$, where $\gamma = 0.577\ldots$ is Euler's number.

Acknowledgments. We thank N. Huang for providing the u_* numbers for the Cox and Munk data and K. Davidson, W. Shaw, C. Friehe, and W. Large for generously providing their wind data from FASINEX. R. Gilmore collected the NOAA gust probe data in MASEX. D. Atlas was responsible for organizing MASEX. E. Dobson kindly provided us with her Geosat data. Funding support was provided by the Studies Program Process Office of NASA Headquarters.

REFERENCES

Adorjan, A. S., and F. A. Wierum, Radiative properties of rough surfaces, *AIAA Journal*, *9*, 2172–2179, 1971.

Banner, M. L., Equilibrium spectra of wind waves, *J. Phys. Oceanogr.*, *20*, 966–984, 1990.

Barrick, D. E., A relationship between the slope probability density function and the physical optics integral in rough surface scattering, *Proc. IEEE*, *36*, 1728–1729, 1968.

Barrick, D. E., Remote sensing of sea state by radar, in *Remote Sensing of the Troposphere*, edited by V. E. Derr, chap. 12, U.S. Government Printing Office, Washington, D. C., 1972.

Barrick, D. E., Wind dependence of quasi-specular microwave sea scatter, *IEEE Trans. Antennas Propag.*, *AP-22*, 135–136, 1974.

Battjes, J. A., T. J. Zitman, and L. J. Holthuijsen, A reanalysis of spectra observed in JONSWAP, *J. Phys. Oceanogr.*, *17*, 1288–1295, 1987.

Beckmann, P., and A. Spizzichino, *The Scattering of Electromagnetic Waves from Rough Surfaces*, 503 pp., Pergamon, New York, 1963.

Brown, G. S., Backscattering from Gaussian-distributed perfectly conducting rough surfaces, *IEEE Trans. Antennas Propag.*, *AP-26*, 472–482, 1978.

Brown, G. S., Estimation of surface wind speeds using satellite-borne radar measurements at normal incidence, *J. Geophys. Res.*, *84*, 3974–3978, 1979.

Brown, G. S., Quasi-specular scattering from the air-sea interface, in *Surface Waves and Fluxes*, vol. 2, edited by W. Plant and G. Geernaert, pp. 1–40, Kluwer Academic, Boston, 1990.

Brown, G. S., H. R. Stanley, and N. A. Roy, The wind speed measurement capability of spaceborne radar altimetry, *IEEE J. Oceanic Eng.*, *OE-6*, 59–63, 1981.

Cardone, V. J., Specification of the wind distribution in the marine boundary layer for wave forecasting, Ph.D. thesis, New York Univ., 1969.

Chalikov, D. V., and V. K. Makin, Models of the wave boundary layer, *Boundary Layer Meteorol.*, *56*, 83–99, 1991.
Chen, M. F., and A. K. Fung, A numerical study of the regions of validity of the Kirchhoff and small-perturbation rough surface scattering methods, *Radio Sci.*, *23*, 163–170, 1988.
Chou, S-H., D. Atlas, and E-N Yeh, Turbulence in a convective marine atmospheric boundary layer, *J. Atmos. Sci.*, *43*, 547–564, 1986.
Cox, C., and W. Munk, Statistics of the sea surface derived from sun glitter, *J. Mar. Res.*, *13*, 198–227, 1954.
Csanady, G. T., Air-sea momentum transfer by means of short-crested wavelets, *J. Phys. Oceanogr.*, *15*, 1486–1501, 1985.
Daley, J. C., The wind dependence of radar sea return, *J. Geophys. Res.*, *78*, 7823–7833, 1973.
Davidson, K. L., W. J. Shaw, and W. L. Large, Wind stress results from multi-platform and multi-sensor measurement in FASINEX, in *Proceedings of the Seventh Conference on Oceans-Atmosphere Interaction*, pp. 132–136, American Meteorological Society, Boston, 1987.
Dobson, E. B., F. Monaldo, and J. Goldhirsh, Validation of Geosat altimeter-derived wind speeds and wave heights using buoy data, *J. Geophys. Res.*, *92*, 10,710–10,731, 1987.
Donelan, M., Air-sea interaction, in *The Sea*, vol. 9, John Wiley, New York, 1990.
Donelan, M., and W. J. Pierson, Jr., Radar scattering and equilibrium ranges in wind-generated waves with application to scatterometry, *J. Geophys. Res.*, *92*, 4971–5029, 1987.
Durden, S. L., and J. F. Vesecky, A physical radar cross section model for a wind driven sea with swell, *IEEE J. Oceanic Eng.*, *OE-16*, 445–450, 1985.
Ebuchi, N., H. Kawamura, and Y. Toba, Growth of wind waves with fetch observed by the Geosat altimeter in the Japan Sea under winter monsoon, *J. Geophys. Res.*, *97*, 809–819, 1992.
Fedor, L. S., and G. S. Brown, Wave height and wind speed measurements from the Seasat radar altimeter, *J. Geophys. Res.*, *87*, 3254–3260, 1982.
Friehe, C. A., W. J. Shaw, D. P. Rogers, K. L. Davidson, W. G. Large, S. A. Stage, G. H. Crescenti, S. J. S. Khalsa, G. K. Greenhut, and F. Li, Air-sea fluxes and surface layer turbulence around a sea surface temperature front, *J. Geophys. Res.*, *96*, 8593–8610, 1991.
Geernaert, G. L., Bulk parameterizations for the wind stress and heat fluxes, in *Surface Waves and Fluxes*, vol. 1, edited by W. Plant and G. Geernaert, pp. 91–172, Kluwer Academic, Boston, 1990.
Haimbach, S. P., and J. Wu, Field trials of an optical scanner for studying sea-surface fine structures, *IEEE J. Oceanic Eng.*, *OE-10*, 452–454, 1985.
Hammond, D. L., R. A. Mennella, and E. J. Walsh, Short pulse radar used to measure sea surface wind speed and SWH, *IEEE Trans. Antennas Propag.*, *AP-25*, 61–66, 1977.
Holliday, D., Resolution of a controversy surrounding the Kirchhoff approach and the small perturbation method in rough surface scattering theory, *IEEE Trans. Antennas Propag.*, *AP-35*, 120–122, 1987.
Hwang, P. A., and O. Shemdin, The dependence of sea surface slope on atmospheric stability and swell conditions, *J. Geophys. Res.*, *93*, 13,903–13,912, 1988.
Jackson, F. C., A curvature-corrected Kirchhoff formulation for radar sea return from the near vertical, Ph.D. thesis, New York Univ., 1972.
Jackson, F. C., The reflection of impulses from a nonlinear random sea, *J. Geophys. Res.*, *84*, 4939–4943, 1979.
Jackson, F., A physically based model of the altimeter wind speed response, Proceedings of WOCE/NASA Altimeter Algorithm Workshop, Corvallis, Oregon, *U.S. WOCE Tech. Rep. 2*, edited by B. Chelton, appendix, U.S. Planning Office for WOCE, College Station, Texas, 1988.
Jackson, F. C., Directional wave spectra from the radar ocean wave spectrometer during LEWEX, in *Directional Ocean Wave Spectra*, edited by R. C. Beal, pp. 91–97, Johns Hopkins University Press, Baltimore, Md., 1991.
Jackson, F. C., W. T. Walton, and P. L. Baker, Aircraft and satellite measurement of ocean wave directional spectra using scanning-beam microwave radars, *J. Geophys. Res.*, *90*, 987–1004, 1985.
Jähne, B., K. O. Munnich, F. Bosinger, A. Dutzi, W. Huber, and P. Libner, On the parameters influencing air-water gas exchange, *J. Geophys. Res.*, *92*, 1937–1950, 1987.
Jähne, B., and K. S. Riemer, Two-dimensional wave number spectra of small-scale water surface waves, *J. Geophys. Res.*, *95*, 11,531–11,546, 1990.
Jannsen, P. A. E. M., P. Lionello and L. Zambresky, On the interaction of wind and waves, *Philos. Trans. R. Soc. London, Ser. A*, *329*, 289–301, 1989.
Jones, W. L., L. C. Schroeder, and J. L. Mitchell, Aircraft measurements of the microwave scattering signature of the ocean, *IEEE J. Oceanic Eng.*, *OE-2*, 53–61, 1977.
Kitaigorodskii, S. A., On the theory of the equilibrium range in the spectrum of wind-generated gravity waves, *J. Phys. Oceanogr.*, *13*, 816–827, 1983.
Kwaii, S. K. Okuda, and Y. Toba, Field data in support of three-seconds power law and $gu_*\sigma^{-4}$ spectral form for growing wind waves, *J. Oceanogr. Soc. Jpn.*, *33*, 137–150, 1977.
Large, W. G., and J. A. Businger, A system for remote measurements of wind stress over the ocean, *J. Atmos. Oceanic Technol.*, *5*, 274–285, 1988.
Large, W. G., and S. Pond, Open ocean momentum flux measurements in moderate to strong winds, *J. Phys. Oceanogr.*, *11*, 324–336, 1981.
Leykin, I. A., and A. D. Rozenberg, Sea-tower measurements of wind-wave spectra in the Caspian Sea, *J. Phys. Oceanogr.*, *14*, 168–176, 1984.
Li, F., W. G. Large, W. Shaw, E. Walsh, and K. Davidson, Ocean backscatter relationship with near surface winds: A case study during FASINEX, *J. Phys. Oceanogr.*, *19*, 342–353, 1989.
Liu, P. C., On the slope of the equilibrium range in the frequency spectrum of wind waves, *J. Geophys. Res.*, *94*, 5017–5023, 1989.
Liu, A. K., F. C. Jackson, E. J. Walsh, and C. Y. Peng, A case study of wave-current interaction near an oceanic front, *J. Geophys. Res.*, *94*, 16,189–16,200, 1989.
Longuet-Higgins, M. S., On the dynamics of steep gravity waves in deep water, in *Turbulent Fluxes Through the Sea Surface, Wave Dynamics and Wave Prediction*, edited by A. Favre and K. Hasselmann, pp. 199–218, Plenum, New York, 1978.
Luke, Y. L., Integrals of Bessel functions, in *Handbook of Mathematical Functions*, edited by M. Abramowitz and I. Stegun, pp. 480–494, Dover, Mineola, New York, 1966.
Masuko, H., K. Okamoto, M. Ahimada, and S. Niwa, Measurement of microwave backscattering signatures of the ocean surface using X band and K_a band airborne scatterometers, *J. Geophys. Res.*, *91*, 13,056–13,083, 1986.
Munk, W., A critical wind speed for air-sea boundary layer processes, *J. Mar. Res.*, *6*, 203–218, 1947.
Munk, W., Wind stress on water: An hypotheses, *Q. J. R. Meteorol. Soc.*, *81*, 320–332, 1955.
Pennington, N. J., and R. A. Weller, Cruise summaries for FASINEX phase two, *Tech. Rep. 86-36*, Woods Hole Oceanography Institute, Woods Hole, Mass., Oct. 1986.
Phillips, O. M., Spectral and statistical properties of the equilibrium range in wind-generated gravity waves, *J. Fluid Mech.*, *156*, 505–531, 1985.
Plant, W. J., A relationship between wind stress and wave slope, *J. Geophys. Res.*, *87*, 1961–1967, 1982.
Plant, W. J., A two-scale model of short wind generated waves and scatterometry, *J. Geophys. Res.*, *91*, 10,735–10,749, 1986.
Resio, D., and W. Perrie, A numerical study of nonlinear energy fluxes due to wave-wave interactions, *J. Fluid Mech.*, *223*, 603–629, 1991.
Rodriguez, E., Beyond Kirchhoff approximation II electromagnetic scattering, *Radio Sci.*, *26*, 121–132, 1991.
Schroeder, L. C., D. H. Boggs, G. Dome, I. M. Halberstam, W. L. Jones, G. J. Dame, W. J. Pierson, and F. J. Wentz, The relationship between wind vector and normalized radar cross section used to derive Seasat-A satellite scatterometer winds, *J. Geophys. Res.*, *87*, 3318–3336, 1982.
Schroeder, L. C., W. L. Jones, P. R. Schaffner, and J. L. Mitchell, Flight measurement and analysis of AFFE RADSCAT wind speed signature of the ocean, *NASA Tech. Memo. 85646*, Jan. 1984.
Schroeder, L. C., P. R. Schaffner, J. L. Mitchell, and W. L. Jones, AAFE RADSCAT 13.9 GHz measurements and analysis: Wind speed signature of the ocean, *IEEE J. Oceanic Eng.*, *OE-10*, 346–357, 1985.

Thompson, D. R., Calculation of radar backscatter modulations from internal waves, *J. Geophys. Res.*, *93*, 12,371–12,380, 1988.

Thompson, T. W., D. E. Weissman, and F. I. Gonzalez, *L* band radar backscatter dependence upon surface wind stress: A summary of new Seasat 1 and aircraft observations, *J. Geophys. Res.*, *88*, 1727–1735, 1983.

Valenzuela, G. R., Theories for the interaction of electromagnetic and oceanic waves—A review, *Boundary Layer Meteorol.*, *13*, 61–85, 1978.

Walsh, E. J., D. W. Hancock III, D. E. Hines, R. N. Swift, and J. F. Scott, Directional wave spectra measured with the Surface Contour Radar, *J. Phys. Oceanogr.*, *15*, 566–592, 1985.

Weissman, D., The dependence of the microwave radar cross section on ocean surface variables: Comparison of measurements and theory using data from the Frontal-Air-Sea Interaction Experiment (FASINEX), *J. Geophys. Res.*, *95*, 3387–3398, 1990.

Weller, R., Overview of the Frontal Air-Sea Interaction Experiment (FASINEX), *J. Geophys. Res.*, *96*, 8501–8516, 1991.

Wentz, F. J., A two-scale scattering model for foam-free sea microwave brightness temperatures, *J. Geophys. Res.*, *80*, 3441–3446, 1975.

Wentz, F. J., Cox and Munk's sea surface slope variance, *J. Geophys. Res.*, *81*, 1607–1608, 1976.

Wentz, F. J., A two scale scattering model with application to the JONSWAP '75 aircraft microwave scatterometer experiment, *NASA Contract. Rep. 2919*, Dec. 1977.

Wilheit, T. T., The effect of wind on the microwave emission from the ocean's surface at 37 GHz, *J. Geophys. Res.*, *84*, 4921–4926, 1979.

Witter, D. L., and D. B. Chelton, A Geosat altimeter wind speed algorithm and a method for altimeter wind speed algorithm, *J. Geophys. Res.*, *96*, 8853–8860, 1991.

Wu, J., Sea-surface slope and equilibrium wind-wave spectra, *Phys. Fluids*, *15*, 741–747, 1972.

Wu, J., Momentum flux from wind to aqueous flows at various wind velocities and fetches, *J. Phys. Oceanogr.*, *18*, 140–144, 1987.

D. E. Hines, NASA Goddard Space Flight Center, Wallops Flight Facility, Code 972, Wallops Island, VA 23337.

F. C. Jackson, Laboratory for Oceans, NASA Goddard Space Flight Center, Code 971, Greenbelt, MD 20771.

C. Y. Peng, Science Systems and Applications, Incorporated, 5900 Princess Garden Parkway, Suite 300, Lanham, MD 20706.

B. A. Walter, Science Applications International Incorporated, 13400 B. Northup Way, Suite 36, Bellevue, WA 98005.

W. T. Walton, Engineering Research Center of the University of Maryland, College Park, MD 20742.

(Received March 12, 1992;
revised April 6, 1992;
accepted April 6, 1992.)